Gravity currents propagating upslope in uniform and two-layer stratified ambients

by

Larissa J. Marleau

A thesis submitted in partial fulfillment of the requirements for the degree of

Master of Science

Department of Mechanical Engineering
University of Alberta

Abstract

Bottom propagating gravity currents resulting from full- and partial-depth lock-release experiments are investigated as they propagate up a rising slope in uniform and two-layer stratified ambients.

In the case of uniform ambients, the gravity current front decelerates in a nearly uniform manner along the slope at a rate that agrees with theoretical predictions. The shape of the gravity current as it decelerates over relatively steep slopes is found to be self-similar with a nearly linear decrease of the head height between the start of the slope and up to 80% of the distance to the nose. Some deviation from self-similar behaviour is found in cases with small slopes because of the comparatively large volume of fluid in the gravity current tail that flows downslope while the front continues to advance upwards.

In the case of two-layer ambients, the initial gravity current front speed is found to be consistent with a theory adapted from Shin *et al.* (2004). The subsequent evolution depends on the gravity current speed relative to the speed of the interfacial disturbance it creates. The deceleration of supercritical gravity currents, which travel faster than the interfacial disturbance, is gradual and agrees well with the relationship developed for upslope gravity currents in uniform density ambients and modified for a two-layer ambient. In most subcritical cases the gravity current suddenly comes to rest as a consequence of interactions with the interfacial disturbance. The disturbance amplitude, speed, and width are found to be nearly constant during its evolution. In cases for which the ambient interface intersected the tank bottom, the amplitude, speed, and width are nearly constant up to the point where the lower layer shallowed and the disturbance transformed into an upslope propagating gravity current.

Preface

Work related to gravity currents propagating in uniform ambients included in Chapters 2, 3, and 4 has been published as L. J. Marleau, M. R. Flynn, and B. R. Sutherland "Gravity currents propagating up a slope," *Physics of Fluids*, vol. 26, 046605. The work related to gravity currents propagating in two-layer stratified ambients in Chapters 2, 3, and 4 is planned to be submitted for publishing as L. J. Marleau, M. R. Flynn, and B. R. Sutherland "Gravity currents propagating up a slope in a two-layer ambient fluid" to *Physics of Fluids.* For both manuscripts, I was responsible for conducting and analyzing the experiments as well as composition of the manuscripts. Bruce R. Sutherland and Morris R. Flynn were fundamental to the formation of the concepts and were the supervisory authors for the manuscript compositions.

To my mom for her unconditional support in my journey to footless halls of air and windswept heights. And to all my pilot friends who created an environment in which I could find myself.

Acknowledgements

Working under supervisors as knowledgable and enthusiastic as Dr. Bruce Sutherland and Dr. Morris Flynn has enabled me to successfully complete this degree while gaining valuable knowledge and skills pertaining to research, academia, and communication. Their insight and advice were invaluable to the progress made. And their phenomenal flexibility with my schedule and sabbaticals allowed me to continue to support youth through work with the Canadian Cadet Movement and to pursue opportunities that will be beneficial in my future career.

My mom and family have continually supported my education alongside my career endeavours. That support did not go unnoticed. Thank-you to Katie for her encouragement, patience, and understanding throughout my degree.

The experimental assistance received from Victor Benitez and Dylan Podkowka was much appreciated. Finally, I would like to acknowledge the financial support from the Natural Sciences and Engineering Research Council through the Discovery Grant and Research Tools and Instruments program.

Contents

List of Tables

List of Figures

Chapter 1

Introduction

A gravity current is a primarily horizontal flow caused by density differences between the current fluid and the ambient fluid (Benjamin (1968); Simpson (1982, 1997); Maxworthy *et al.* (2002)). Some examples of gravity currents found in nature are thunderstorm outflows, sea breezes, dust storms (haboobs), salt wedges in estuaries and advancing cold fronts. Gravity currents are also found in industrial processes in the spread of heavy gases and buoyancy driven ventilation systems (Simpson (1997)). Many studies have investigated gravity currents by way of theory, laboratory experiments, and numerical simulations for the special case in which the gravity current travelled along a horizontal surface (Keulegan (1957, 1958); Benjamin (1968); Simpson (1972); Huppert & Simpson (1980); Huppert (1982); Rottman & Simpson (1983); Shin *et al.* (2004); Borden & Meiburg (2013)) or over small obstacles (Lane-Serff *et al.* (1995); Baines (1984)).

To predict the speed of a gravity current, Benjamin (1968) used a reference frame fixed to the gravity current front and required mass and momentum conservation. This model allowed him to derive a formula for the gravity current speed with respect to the height of the gravity current, the height of the ambient fluid, and the density difference between the two fluids. By additionally assuming energy conservation, he showed that the gravity current head should occupy half of the ambient depth. The prediction was confirmed by the results of full-depth lock-release experiments (Shin *et al.* (2004)). Through experiments with finite-length locks and using a theory that combined Benjamin's front condition with shallow water theory, Rottman & Simpson (1983) showed that a full-depth lock-release gravity current that initially spans the depth of the ambient propagates six to ten lock-lengths at a constant speed. The flow then transitions from the slumping phase to a self-similar phase for which the front speed decreases as a function of time (Huppert (1982); Rottman & Simpson (1983); Ungarish (2009)). Among several investigations of gravity currents arising from partial-depth lock-release experiments, Shin *et al.* (2004) adapted Benjamin's theory to account for the return flow into the lock. By applying the unsteady, rather than the steady, form of Bernoulli's equation, they developed a prediction for the speed of an energy conserving gravity current and found their prediction to be consistent with experimental measurements. All of the studies cited thus far were investigations of the case of a uniform ambient and a horizontal bottom.

Relatively few laboratory studies have been conducted of gravity currents moving over a non-horizontal bottom or over obstacles (Britter & Linden (1980); Meiburg & Kneller (2010); Cenedese & Adduce (2008); Dai (2013, 2014)). Britter & Linden (1980) show that, even for small downslope angles, the current resulting from a constant volume-flux source propagated at constant speed far downstream as a result of the balance between gravity, that accelerates the flow, and basal friction and entrainment, which have a retarding influence. In contrast, upslope propagating gravity currents in uniform ambients decelerate (Adduce *et al.* (2014)). One of the very few studies of gravity currents propagating upslope was performed by Adduce *et al.* (2014) who conducted experiments to investigate bottom propagating gravity currents on upsloping beds with slopes ranging from 0 to 0.027 to study the accuracy of numerical entrainment models. Their code, which solved the two-layer shallow water equations, was an extension of an earlier study of horizontally propagating currents (Adduce *et al.* (2012)).

Several studies have considered horizontally propagating gravity currents in stratified ambients (Holyer & Huppert (1980); Flynn *et al.* (2012); Sutherland *et al.* (2004); Tan *et al.* (2010); Adduce *et al.* (2012)). In experiments of intrusive gravity currents in two-layer, three-layer, and uniformly stratified fluids, the currents were observed to excite internal waves that then acted upon the currents causing them to halt abruptly or, in symmetric circumstances, propagate long distances at constant speed (Sutherland *et al.* (2004); Mehta *et al.* (2002); Munroe *et al.* (2009)). Rottman & Simpson (1989) compared a gravity current moving over a horizontal bottom beneath a two-layer ambient to a symmetric, streamlined obstacle being towed beneath a two-layer ambient, as was studied by Baines (1984). Comparing their theory to laboratory experiments, Rottman & Simpson found that interfacial disturbances created by gravity currents took on qualitatively different forms depending on the bore speed and initial conditions of the lock-release experiments.

The purpose of this investigation is to examine the evolution of bottom propagating gravity currents in uniform and two-layer stratified ambients as they encounter a rising uniform slope. Included within the scope of uniform ambient cases are gravity currents produced by full- and partial-depth lock-release that propagate over slopes ranging from moderately shallow to steep. The scope of two-layer ambient cases is limited to a range of partial-depth locks and shallow slopes. Besides the fundamental interest in exploring how fast and how far the current moves upslope, this research also provides insight into the evolution of sea breezes as they advance inland and uphill from the coast in the presence of an atmospheric inversion. This research more broadly constitutes the start of a theoretical and laboratory experimental program investigating the advance of sea breezes over complex coastal terrain in order to provide a better understanding of their impact upon vegetation, industry, and communities. An example of an agricultural application is the influence of sea breezes that bring moisture and cooler temperatures to the inland wineries near Santa Barbara, California.

In Chapter 2, existing theories for gravity currents in uniform-depth ambients are adapted using a WKB-type analysis so as to predict how the front position changes in time when flowing up a shallow slope. Also, predictions for the gravity current speed, upslope deceleration and stopping distance are extended to the case of a two-layer ambient. Predictions for the amplitude of the interfacial disturbances excited by the impinging gravity current are reviewed. Chapter 3 describes the set-up of the lock-release experiments, the image processing algorithms and analyses used to extract quantitative data from laboratory images. Qualitative observations of the formation and evolution of the gravity current and of the interfacial disturbance are also described here. Chapter 4 presents a quantitative comparison of measurements of the gravity current front speed against theoretical predictions and the interfacial disturbance speed. The deceleration and stopping distance of gravity currents are examined. Moreover, the measured interfacial disturbance amplitudes are compared to predictions and the dependance of disturbance width and speed upon amplitude is examined. Chapter 5 gives a summary of key results and outlines ideas for future research.

Chapter 2

Theory

2.1 Horizontal Front Speed in a Uniform Ambient

Within this investigation the speed, U_{GC}, of an inviscid, steady-state gravity current propagating over a horizontal surface in an ambient fluid of depth H, is written in terms of a Froude number, Fr_H, by $U_{GC} = \mathrm{Fr}_H\sqrt{g'H}$, in which $g' \equiv g(\rho_0 - \rho_2)/\rho_{00}$ is the reduced gravity based on the current and ambient densities, ρ_0 and ρ_2, respectively. In the Boussinesq approximation, ρ_{00} is a reference density taken to be any value between ρ_2 and ρ_0. Benjamin's steady-state analysis (Benjamin (1968)) predicted $\mathrm{Fr}_H = [\delta(1-\delta)(2-\delta)/(1+\delta)]^{1/2}$ in which $\delta \equiv d/H$ is the ratio of the gravity current height, d, to the ambient depth. Additionally, assuming energy conservation, he found that $\delta = d/H = 1/2$ for which $\mathrm{Fr} = 1/2$. This prediction was reasonably well borne out in full-depth lock-release experiments (Lowe *et al.* (2002); Shin *et al.* (2004)), which found $\delta \simeq 0.5$ and $\mathrm{Fr}_H \simeq 0.45$. The minor discrepancy in Fr_H between theory and experiment indicated that the energy loss associated with mixing was a small fraction of the kinetic and available potential energies of the flow (Shin *et al.* (2004); Borden & Meiburg (2013)). Benjamin (1968) also predicted the speed of a steady gravity current in an infinitely deep ambient to be $U_{GC} = \sqrt{2g'd}$. However, because his theory did not explicitly take into consideration the initial conditions, it was unable to give a deterministic prediction for the speed of partial-depth lock-release gravity currents.

By considering the return flow into the lock as well as the advancing gravity current head, Shin *et al.* (2004) extended Benjamin's analysis to predict the speed of energy conserving gravity currents released from partial-depth locks. In particular, Shin *et al.* (2004) predicted the current depth to be $d = D/2$, where D is the initial depth of the gravity current fluid inside the lock. By extension, they predicted the front speed to be

$$U_{GC} = \mathrm{Fr}\sqrt{g'H} \tag{2.1}$$

where

$$\mathrm{Fr} = \sqrt{\delta(1-\delta)}. \tag{2.2}$$

Explicitly, considering the limit $D \to H$, it can be seen that $\mathrm{Fr} \to \mathrm{Fr}_H$ for the case of energy conserving gravity currents. Thus the predictions for both d and U_{GC} reduced to those of Benjamin (1968) for full-depth lock-release currents ($D = H$). However, in the limit $D \ll H$, they found $U_{GC}/\sqrt{g'd} = 1$ instead of $\sqrt{2}$. Though their theory involved the simplifying assumptions of energy conservation and negligible vertical accelerations, its predictions were in strong agreement with the results of laboratory experiments (e.g. see Figure 14 of Shin *et al.* (2004)).

Both Benjamin (1968) and Shin *et al.* (2004) assumed that $\mathrm{Re} \gg 1$ so that the kinematic viscosity of the fluid, ν, had a negligible effect on the average velocity of the gravity current. The same assumption is used in this investigation and holds true provided that neither D/H nor g' is very small. Viscosity is known to affect instabilities that develop along the current front and consequent mixing behind the head. Experiments have shown, however, that these instabilities exert little influence upon the mean advance of the current head (Härtel *et al.* (2000)), which also explains the success of two-dimensional numerical simulations in modelling the bulk features of the flow.

2.2 Upslope Deceleration in a Uniform Ambient

To predict how the current front slows down over the slope, a WKB-like approach is taken.[1] This is similar to that used by Sutherland *et al.* (2013*b*), who examined surface gravity currents shoaling over sloping topography. It is assumed that the front deceleration along the slope is caused only by the decreasing ambient fluid height; the influence of the along-slope component of gravity is ignored. The Froude number is assumed to be a constant, $\mathrm{Fr} = F_0$, while the current propagates upslope into an ambient of decreasing height, $H_s(x)$, where x denotes the horizontal coordinate. This assumption is equivalent to the requirement that the ratio of the current height to the ambient depth remains constant throughout the upslope propagation (see §11.6.4 of Simpson (1997)). Together with (2.1), in which $U_{GC} \equiv \mathrm{d}x/\mathrm{d}t$, the above considerations lead to

$$\frac{\mathrm{d}x}{\mathrm{d}t} = F_0 \left(g' H_s(x)\right)^{1/2}. \tag{2.3}$$

For the case of a uniform slope, $H_s(x) = H - sx$ for $x > 0$, the solution of (2.3) is

$$x(t) = -\tfrac{1}{4} F_0^2 g' s t^2 + U_{GC} t, \tag{2.4}$$

in which U_{GC} is the speed of the incident current when it first encounters the slope at $t = 0$. Therefore the current should undergo

---

[1] WKB are the initials of Wentzel, Kramers, and Brillouin, who applied their mathematical method to problems in quantum mechanics.

a constant deceleration whose horizontal component has magnitude $d_x = F_0^2 g's/2$. Using (2.2), this is given in terms of D and H by

$$d_x = \tfrac{1}{2}g's\delta(1-\delta) = \tfrac{1}{8}g's\frac{D}{H}\left(2 - \frac{D}{H}\right). \tag{2.5}$$

In particular, for full-depth lock-release currents ($D/H = 1$), $d_x = g's/8$. For any value of D/H, the maximum horizontal distance traversed by the gravity current as it runs upslope is

$$x_{\max} = \frac{U_{GC}^2}{\delta(1-\delta)g's} = \frac{H}{s}, \tag{2.6}$$

in which the latter expression is derived using (2.1). The corresponding maximum height measured from the tank bottom is $z_{\max} = sx_{\max} = H$.

As a gravity current encounters and then rises up a slope, its velocity must decrease as its kinetic energy is converted to potential energy. Heuristically one might expect the current to rise upslope a vertical distance D, equal to its initial height in the lock. Assuming the current undergoes a constant deceleration as it rises upslope and that it stops at a vertical height D, the horizontal deceleration is predicted to be

$$d_x = \frac{U_{GC}^2}{2(D/s)} = \tfrac{1}{8}g's\left(2 - \frac{D}{H}\right). \tag{2.7}$$

Predictions (2.5) and (2.7) will be tested through lab experiments.

2.3 Initial Speed in a Two-Layer Stratified Ambient

For the initial front speed in a two-layer stratified ambient, an adaptation of the Shin *et al.* (2004) prediction result is used. The upper-layer ambient depth and density are $H - h$ and ρ_2, respectively, and the lower-layer depth and density are h and ρ_1, respectively. We suppose that a gravity current results from the release of lock-fluid having density ρ_0 ($> \rho_1 > \rho_2$) and depth D ($> h$) above the bottom. The depth-weighted mean density of the ambient fluid outside the lock from the bottom to height D is $\overline{\rho} = (1 - h/D)\rho_2 + (h/D)\rho_1$. It is assumed that the initial front speed is set by the density difference between the lock-fluid and $\overline{\rho}$, as expressed through the reduced gravity by $\overline{g}' = g(\rho_0 - \overline{\rho})/\rho_{00}$. Thus, using (2.1) and (2.2) it is predicted

$$U_{GC} = \frac{1}{2}\sqrt{\frac{S}{\kappa}(2H - D)g'_{02}}, \tag{2.8}$$

where $S = (\rho_1 - \rho_2)/(\rho_0 - \rho_2)$ is the stratification parameter introduced by Ungarish (2009), $g'_{02} = g(\rho_0 - \rho_2)/\rho_2$ is the reduced gravity based on the lock-fluid and upper-layer ambient density, and $\kappa = HS/(D - hS)$. This prediction will be compared with experimental results.

2.4 Upslope Deceleration and Stopping Distance in a Two-Layer Stratified Ambient

Although the above result is derived in the limit of negligibly small slope angles ($\theta \to 0$), it should remain applicable in the case of small θ at early times. For longer times, the front is expected to decelerate at least in part as a consequence of running upslope against gravity, but also as a consequence of the changing relative depths of the upper and lower layer fluids. The result of deceleration in a uniform ambient is readily adapted here by replacing g' in (2.3) with $\overline{g}' = g(\rho_0 - \overline{\rho})/\rho_{00}$ as in (2.8), but now accounting for the linearly decreasing lower-layer depth with x for a current rising upon a uniform slope:

$$\overline{\rho}(x) = \left(1 - \frac{h - sx}{D}\right) \rho_2 \ + \ \frac{h - sx}{D} \rho_1. \tag{2.9}$$

Hence the speed as a function of distance is written as

$$\frac{\mathrm{d}x}{\mathrm{d}t} = F_0 \left(\overline{g}'(x) H_s(x)\right)^{1/2}. \tag{2.10}$$

in which F_0 is given by (2.2), $H_s(x) = H - sx$ and the co-ordinate system is defined so that $x = 0$ corresponds to where the current speed is U_{GC}, given by (2.8). Equation (2.10) can be integrated to obtain an expression for the front position, x, in terms of time:

$$x(t) = \frac{H}{2s\kappa}\left[\kappa - 1 + (\kappa + 1)\sin\left(\frac{s}{2H}\sqrt{S(2H - D)g'_{02}}\ t + C\right)\right]. \tag{2.11}$$

The constant C is determined from the initial condition $x(0) = 0$:

$$C = \sin^{-1}\left(\frac{1 - \kappa}{\kappa + 1}\right).$$

The maximum deceleration determined from (2.11) is:

$$d_x = \frac{1}{8} g'_{02} s \left(\frac{D}{H} + S(1 - h/H)\right)\left(2 - \frac{D}{H}\right). \tag{2.12}$$

Using the prediction (2.11), the maximum upslope distance is found to be

$$x_{\max} = \frac{H}{s}. \tag{2.13}$$

This result is obviously unphysical in the case of small D. Under the assumption that the deceleration is constant and equal to (2.12), the maximum distance is found to be

$$x_{\max} = \frac{H}{s}\left(\frac{1}{1 + \kappa}\right). \tag{2.14}$$

The influence of interfacial disturbances generated by the gravity current in a two-layer ambient is neglected in (2.6). As will be argued in Chapter 4, the impact of these disturbances can be substantial if the initial current speed is much slower than the disturbance speed.

2.5 Interfacial Disturbance Amplitude a Two-Layer Stratified Ambient

Tan *et al.* (2010) predicted the amplitude, A, of the ambient interfacial disturbance caused by a partial-depth lock-release gravity current propagating along a horizontal bottom through a two-layer stratified ambient with upper-layer depth $H - h$ and lower-layer depth h. By first applying Bernoulli's equation in the upper and lower ambient layers for the full-depth lock-release case ($D = H$), they found that $A = \frac{1}{2}(H - h)$. In that case it is known that the current depth is half the ambient depth: $d = H/2$. Thus the amplitude of the interfacial disturbance resulting from a full-depth lock-release can be written

$$A = \frac{d}{H}(H - h). \tag{2.15}$$

Assuming d/D decreases linearly as D/H increases, consistent with the experimental data of Rottman & Simpson (1983), and requiring $d = H/2$ when $D = H$, the current depth as a function of lock-depth is estimated to be

$$d = D\left[\alpha - (\alpha - \tfrac{1}{2})\frac{D}{H}\right], \tag{2.16}$$

where $\alpha \simeq 0.87$ is a fitting parameter determined from figure 10 of Rottman & Simpson (1983). Combining (2.16) with the limiting cases of (2.15) gives the prediction for the relative interfacial disturbance amplitude, nondimensionalized by the harmonic mean of the ambient layer depths, $\overline{H} = h(H-h)/H$:

$$\frac{A}{\overline{H}} = \frac{D}{h}\left[\alpha - (\alpha - \tfrac{1}{2})\frac{D}{H}\right]. \tag{2.17}$$

Chapter 3

Experimental Set-up and Observations

The set-up for the uniform ambient and two-layer stratified ambient experiments is illustrated in figure 3.1. Experiments were performed in a long rectangular glass tank of interior length $L = 197.5$ cm, width 17.6 cm, and total height 48.5 cm.

The Reynolds number was based on the lock-depth and density difference between the lock-fluid and the lower layer ambient, so that $\mathrm{Re} = D\sqrt{g'_{02}D}/\nu$, in which ν ($\simeq 0.01\,\mathrm{cm}^2/\mathrm{s}$ for water) is the kinematic viscosity. In our experiments, Re ranged between $\mathrm{Re} = 6 \times 10^3$ and 1.3×10^5, sufficiently large that viscous dissipation was not expected to play a dominant role.

For all of the experiments, a bank of fluorescent bulbs was placed behind the tank. Two translucent white plastic sheets were placed between the lights and the tank to provide nearly uniform background illumination. Movies of the experiments were recorded using a Canon EOS Rebel T3i digital camera. This was situated approximately 3 m in front of the tank, midway along its length, and midway between the free surface and bottom of the tank. The field-of-view was set so that the entire tank length, including the lock region, was included. All densities were measured using an

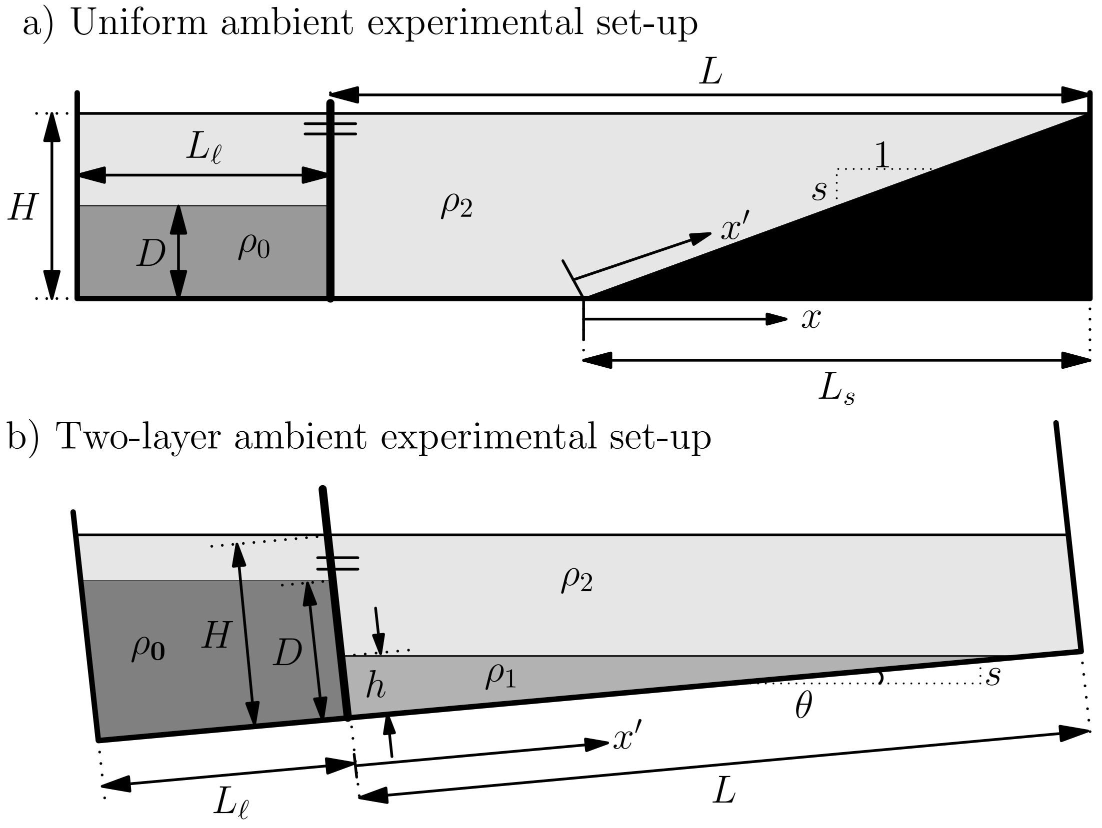

Figure 3.1: Schematic side-view of the laboratory set-up before the start of an experiment. a) Uniform ambient experiment with lock-fluid of density ρ_0 and depth D (dark grey) located behind a gate in a lock of length L_ℓ. The ambient fluid is fresh water with density ρ_2 and depth H (white). b) Two-layer ambient experiment with lock-fluid of density ρ_0 and lock-gate depth D (dark grey). The lower layer ambient fluid is salt water with density ρ_1 and lock-gate depth h (medium grey). The upper ambient fluid is fresh water with density ρ_2 and depth $H - h$ (light grey). The tank is angled such that the bottom surface has slope s, which is here exaggerated for clarity. The gate is orientated normal to the tank bottom.

Anton Paar DMA 4500 density meter, which had a precision of $\pm 0.00001\,\mathrm{g/cm^3}$.

3.1 Uniform Ambient Experimental Set-up

For all uniform ambient cases, the tank was initially filled with fresh water to a height of at least $H = 30.0\,\mathrm{cm}$. A rigid plastic sheet, which acted as a false bottom spanning the tank width, was then inserted with one end at the surface at the right end of the tank and the other end touching the bottom a distance L_s from the right wall. L_s ranged from 26.5 cm to 120.3 cm depending upon the length of the plastic sheet used. The resulting constant slope, s, ranged from 0.25 to 1.13. The precision fit of the sheet pressing against the tank sidewalls held it in place during the set-up and execution of the experiment.

Uniform ambient experiments were performed with gravity currents released from either full- or partial-depth locks. In the former case, a water-tight gate was inserted into a vertical track located a distance $L_\ell = 28.4\,\mathrm{cm}$ from the left wall of the tank. Thus the lock spanned approximately 1/6 the tank length. Because a gravity current is expected to propagate at constant speed for at least six lock-lengths along a horizontal bottom (Rottman & Simpson (1983)), any deceleration of the gravity current observed in the experiments was attributed to upslope propagation. Indeed, in four experiments conducted with the slope placed closer to the lock, the results were identical even when $L - L_s$ was reduced by half.

After the gate was inserted, a predetermined mass of salt was mixed into the lock and the resulting lock density, ρ_0. The lock density ranged from $1.0010\,\mathrm{g/cm^3}$ to $1.0500\,\mathrm{g/cm^3}$ whereas the ambient fresh water typically had a density of $0.9985\,\mathrm{g/cm^3}$.

The lock-fluid was dyed with a small amount of food colouring for the purposes of flow visualization. The majority of the experiments were run with moderately small values of s, and with relatively small values of g'_{02}. The experiments conducted with larger values of s and g'_{02}, though less directly applicable to environmental flows, served to validate the predictions for current speed and deceleration over a broad range of parameter space.

Uniform ambient partial-depth lock-release experiments were run using a similar procedure to the one described above. However, for these experiments the gate contained an aperture located just below the free surface which was covered with a sponge and initially sealed. Salt was mixed into the lock-fluid as in the full-depth lock-release experiments. The seal was then removed from the aperture and salty fluid was slowly siphoned out of the bottom of the lock. Replacing the extracted salt water, fresh ambient fluid flowed through the aperture into the top of the lock. The sponge served to minimize mixing between the fresh and salt water layers. Siphoning continued until the salt water in the lock fell to its desired depth, D, measured to an accuracy of 1 cm (figure 3.1). Partial-depth experiments were performed with $D/H = 0.50$ and 0.75. Experiments with lower values of D/H (i.e. 0.25) were not considered because viscous effects would have been non-negligible.

3.2 Stratified Ambient Experimental Set-up

The two-layer ambient experiments required a slightly different set-up procedure. In some experiments the tank was laid flat but in most instances one end of the tank was raised so that the bottom slope was $s = 0.026$ ($\theta = 1.5°$), $s = 0.052$ ($\theta = 3.0°$), or $s = 0.079$ ($\theta = 4.5°$).

First the tank was filled with dyed salt water of density ρ_1 to a height $h = 10.0\,\mathrm{cm}$, as measured at a distance $L_\ell = 40.0\,\mathrm{cm}$ from the left end wall of the tank. A watertight gate was then inserted at this position and fresh water having density ρ_2 was slowly added to the ambient region through a sponge float, which was used to decrease mixing at the interface between the fresh and salt water layers. The resulting interface thickness was typically 0.5 cm, sufficiently thin to approximate the ambient as a two-layer fluid. Simultaneously fresh water was slowly poured into the lock so that the total fluid depths on either side of the gate were approximately equal. The addition of fluid was continued until the free surface inside and outside of the lock was just below a series of sponge-covered perforations that were located 20 cm above the bottom of the gate. Salt and dye were then mixed into the lock so that the resulting lock-fluid density was $\rho_0 > \rho_1$. Thereafter, more fresh water was added to the ambient fluid so that the ambient free surface rose above the level of the perforations, flowed into the lock through the perforations and overlaid the dense lock-fluid. Concurrently, dense fluid was slowly siphoned out of the lock at the same rate as fluid was added, until the dense layer had the prescribed depth, D. Once the filling process was complete, the siphon and sponge float were removed. At this point, both the lock and ambient fluid had a total height H at the position of the lock-gate.

All two-layer experiments were of partial-depth type. D ranged from 10 cm to 20 cm and H was fixed at 30.0 cm. Because $\theta \leq 4.5°$ in all cases, the fluid depths measured perpendicular to the sloped bottom were approximately equal to the corresponding vertical depths. For example, although H was measured as the distance from the bottom of the gate to where the surface meets the gate (see figure 3.1), its value taken to represent the approximate vertical distance from the bottom of the gate to the surface.

The lock density, ρ_0, ranged from 1.0020 g/cm^3 to 1.0200 g/cm^3. The lower-layer ambient density, ρ_1, ranged from 1.0005 g/cm^3 to 1.0100 g/cm^3, in all cases being less than the lock density. Finally, the upper layer had an average density of 0.9986 g/cm^3.

3.3 Uniform Ambient Observations

At the beginning of each experiment, the gate was swiftly extracted. The dense lock-fluid collapsed into the ambient and travelled as a classical gravity current moving along the horizontal bottom of the tank at constant speed until reaching the slope. Thereafter, the current progressed up the slope in the x'-direction with $x = x' = 0$ denoting the base of the slope (see figure 3.1 a). During this deceleration, particularly for the shallow-slope experiments, a progressively larger portion of the fluid fell back down the slope while the ever-thinning gravity current front continued to propagate in the positive x' direction. The gravity current front eventually stopped and subsequently ran back down the slope.

Figure 3.2 shows the evolution of a gravity current in a typical full-depth lock-release experiment. Panels a, b, and c show snapshots of the experiment at times prior to the removal of the gate, during horizontal propagation upon first reaching the slope, and during upslope propagation, respectively. Figure 3.2 b shows that the head height of the gravity current over the horizontal surface is approximately half the ambient depth, as predicted from Benjamin's energy conserving theory. Figure 3.2 c shows that the shape of the gravity current thins as it propagates upslope. This evolution was common for all experiments.

To evaluate the position of the gravity current front, time-series

a) Snapshot at Start of Experiment (t= -10 s)

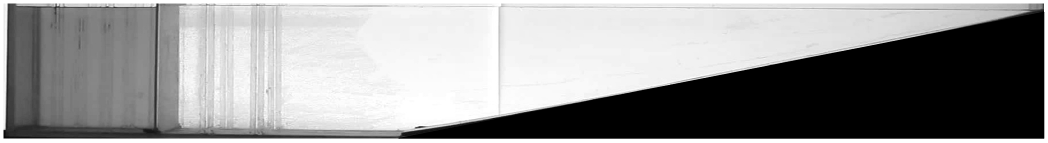

b) Snapshot at t = 0

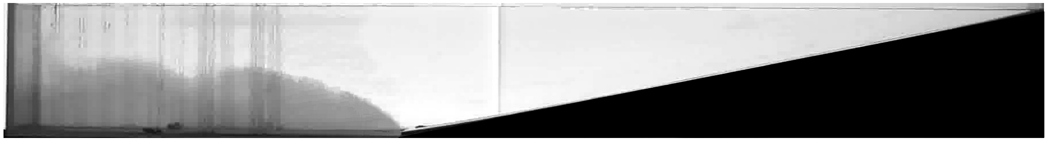

c) Snapshot at t = 30 s

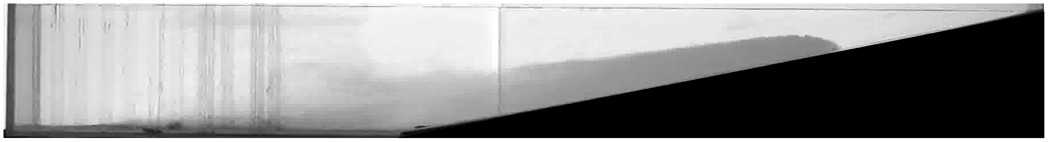

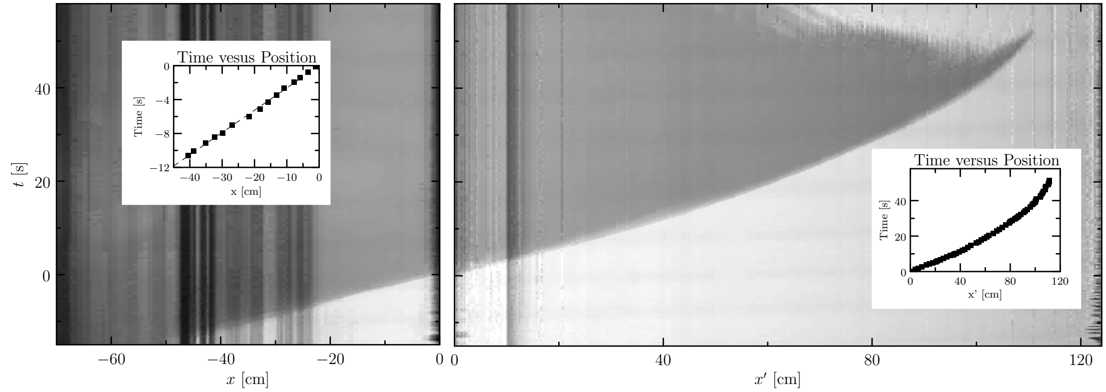

d) Horizontal Time-Series at $z = 1\,\mathrm{cm}$

e) Along Slope Time-Series

Figure 3.2: Results of a full-depth lock-release experiment with $D = H = 30.0\,\mathrm{cm}$, $\rho_0 = 1.001\,\mathrm{g/cm^3}$ and $s = 0.25$. Snapshots show the gravity current at times a) t = -10 s, b) 0 s, and c) 30 s with fields-of-view measuring 197.5 cm long by 30.2 cm tall. d) Front position as a function of time, t, prior to encountering the slope shown as a horizontal time-series and a plot of the extracted data points with the dashed least-squares best-fit line (inset). e) Front position as a function of time as the gravity current propagated upslope shown as a diagonal time-series and a plot of the extracted data points overlying the dashed least-squares best-fit quadratic curve (inset).

were constructed from movies of the experiments. Horizontal time-series were generated by extracting horizontal slices from successive frames, the slice being located 1 cm above the bottom of the tank so as to avoid including in the image any fluid that had leaked from the lock prior to the gate extraction. The slices spanned a horizontal distance $L_\ell + L - L_s$ from the left end wall of the tank. Diagonal time-series were constructed from diagonal slices taken 0.5 cm above the sloping false-bottom. The slices in question began at the tank bottom, ran along the sloping line segment $x' = x\sqrt{s^2+1}$, and ended at the free surface. Results were plotted with the horizontal co-ordinate system having $x < 0$ before the slope and $x' > 0$ along the slope (figure 3.2 d, e). By convention, time was set so that the front reached the base of the slope (at $x = x' = 0$) at time $t = 0$.

Using the horizontal and diagonal time-series from each experiment, data points were extracted and used to create graphs of time versus front position (insets figure 3.2 d, e). The data points were obtained by visually identifying the interface between the dyed lock-fluid and the clear ambient. In cases for which the location of the interface was unclear, its position was estimated to be where the dye had an intensity approximately equal to the average dye intensity of the ambient and lock-fluids.

The initial front speed, U_{GC}, of the gravity current as it approached the slope was found from the slope of the least-squares best-fit line through the data points of x versus t for the nose position taken from the horizontal time-series image. For example, from the best-fit line through the data shown in figure 3.2 d (inset), it was found that $U_{GC} = 3.74\,\mathrm{cm/s}$. The corresponding Froude number was 0.45 for this experiment.

The deceleration of the front was found from the least-squares best-fit quadratic that was fit to the data points corresponding to

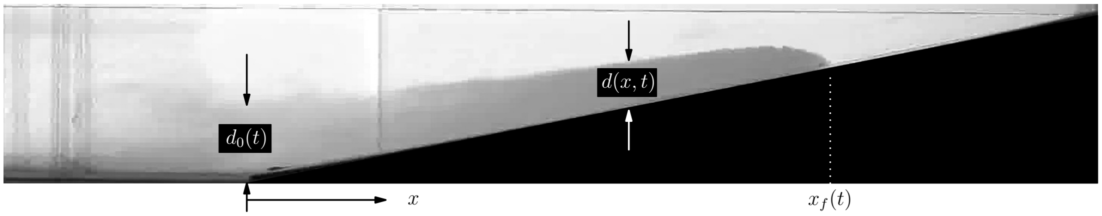

Figure 3.3: Schematic indicating variables used to nondimensionalize the gravity current shape.

the current front in the diagonal time-series. Explicitly, the along-slope deceleration, $d_{x'}$, was set to be twice the coefficient of the t^2 term and the horizontal component of this deceleration was set to be $d_x = d_{x'}/\sqrt{s^2+1}$. For example, from the data shown in figure 3.2 e (inset) the along-slope deceleration was found to be $d_{x'} = 0.062\,\mathrm{cm/s^2}$ and the horizontal deceleration was found to be $d_x = 0.060\,\mathrm{cm/s^2}$.

The evolving shape of the gravity current head between the nose and the base of the slope was examined by comparing the profiles of gravity current height above the slope, $d(x,t)$, measured at five equally spaced times, where $t_{\max}$ corresponds to the point where the front ceased moving upslope. For each value of t, $d(x,t)$ was measured at twenty horizontal positions, x, over the slope. The function was then rescaled first by dividing h by the gravity current height at the base of the slope, $d_0(t)$, and then by dividing x by the front position $x_f(t)$. These definitions of d, d_0, and x_f are illustrated in figure 3.3.

3.4 Two-Layer Ambient Observations

Each experiment began, as in the uniform ambient case, by swiftly extracting the gate. The dense lock-fluid then collapsed beneath the lower-layer ambient as a gravity current. Typically, the collapse also generated a large hump-shaped interfacial disturbance ahead and above the developing gravity current. The disturbance resembled a solitary wave except that dense lock-fluid appeared, at least at early times, beneath the crest of the disturbance. As the gravity current propagated upslope a progressively greater volume of dense fluid drained back toward the lock. In part this was due to gravity. But in many experiments the draining was also influenced by a transfer of momentum between the current and the interfacial disturbance.

In order to measure the evolving structures of both the gravity current and the interfacial disturbance, along-slope time-series plots of gravity current height and interface displacement were constructed for each experiment. The construction was performed using Matlab, which located in each video frame the interface between the two ambient layers and the interface between the current and lower-layer ambient. From these images, the height of the gravity current above the tank bottom and the interface displacement were computed as functions of the along-slope distance, x', from the lock-gate. In practise, these heights were computed for x' in the range $0.5L_\ell < x' < L - 0.5L_\ell$. This interval was chosen because it deliberately excluded the initial collapse of the gravity current and the initial formation of the interfacial disturbance. It also excluded the interaction of the interfacial disturbance and/or the gravity current with the right end wall. The above process was repeated at successive times to produce time series of gravity current height and interface displacement as functions of along-slope distance and time. From the slope of contours in these plots, the speeds of the gravity current and interfacial disturbance, U_{GC} and U_{ID}, were computed. Details of how these speeds were measured are given at the end of this section.

a) Snapshot of a supercritical gravity current at t = 20 s

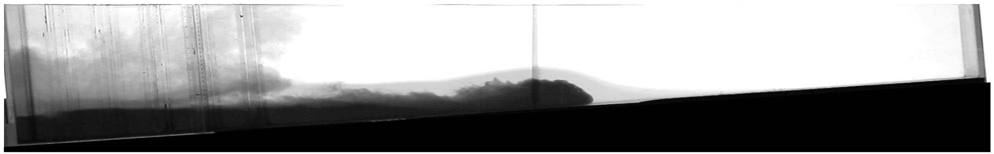

b) Gravity current height

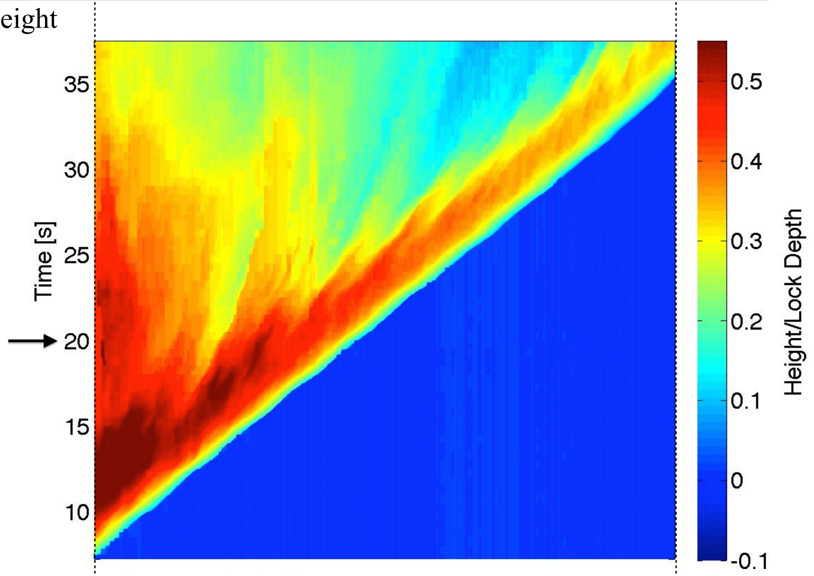

c) Interface displacement

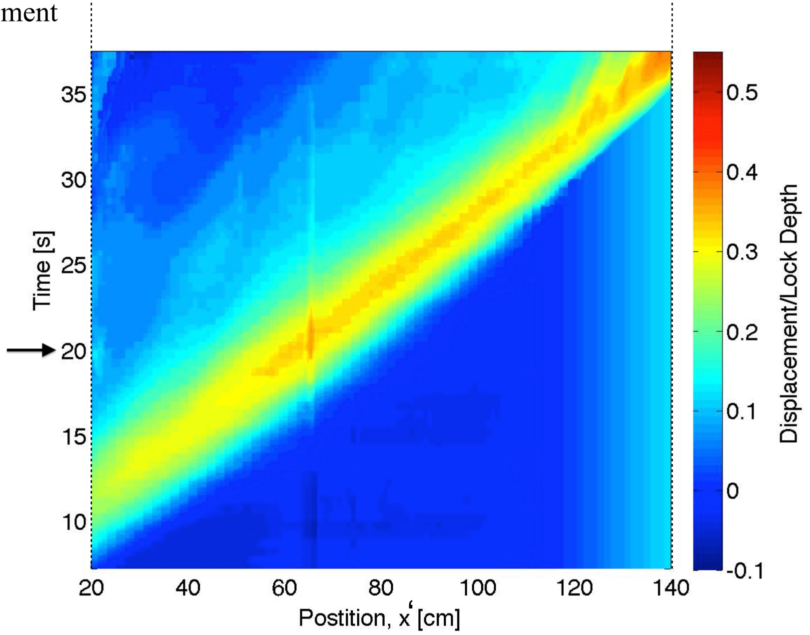

Figure 3.4: [Color] Supercritical experiment snapshot with the field-of-view showing the entire tank (a), gravity current height (b), and interface displacement (c). The arrows at $t = 20\,\mathrm{s}$ in panels b and c indicate the time of the snapshot in panel a. The experimental parameters were $D/H = 0.47$, $s = 0.079$ ($\theta = 4.5°$), $\rho_0 = 1.0064\,\mathrm{g/cm^3}$, $\rho_1 = 1.0014\,\mathrm{g/cm^3}$, and $S = 0.36$. The apparent vertical line at $x' \simeq 65\,\mathrm{cm}$, is the result of the seam between the two plastic sheets behind the tank.

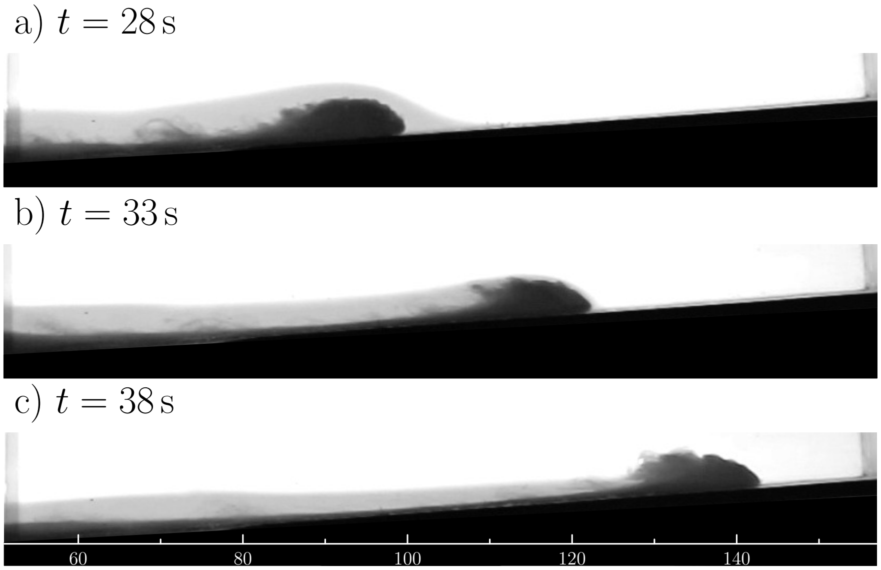

a) $t = 28\,\mathrm{s}$

b) $t = 33\,\mathrm{s}$

c) $t = 38\,\mathrm{s}$

Figure 3.5: Close-up snapshots of the supercritical gravity current shown in figure 3.4 at times (a) t = 28 s, (b) 33 s, and (c) 38 s. The field-of-view shows a portion of the tank close to the right end wall; the scale below panel c indicates the horizontal position from the lock-gate in cm.

The experiments showed different qualitative behaviours depending upon the speed of the gravity current relative to the interfacial disturbance. In an effort to objectively group gravity currents with similar qualitative properties, the gravity currents were classified as subcritical, critical, or supercritical depending on their speed relative to the interfacial disturbance speed. Explicitly, gravity currents were called supercritical if $U_{GC} > 1.04U_{ID}$, subcritical if $U_{GC} < 0.96U_{ID}$, and critical otherwise.

For example, figure 3.4 shows the results of a supercritical gravity current experiment. Panel a presents a snapshot of the experiment taken 20 s after the gate was extracted (at $t = 0$). Here the dark-dyed current is seen to underlie the interfacial disturbance between the clear fresh and light-dyed lower ambient layer. Figure 3.4 b shows a colour contour plot of the gravity current height, $d(x', t)$, nondimensionalized by the lock-depth, D. As expected, the maximum height was approximately $D/2$ shortly after release. At early times the gravity current front maintained a nearly constant speed as it propagated upslope. This is evident from the near-constant slope of the $d \simeq 0.3D$ contour in figure 3.4 b. While rising on the slope, the gravity current head decreased in height and length as the dark-dyed fluid continually drained downslope. Figure 3.4 c shows the displacement of the interface nondimensionalized by D. This panel indicates that, shortly after generation, the interfacial disturbance travelled with a near-constant speed, amplitude, and width even as the gravity current advanced to the leading edge of the disturbance, at which point the gravity current depth and interface displacement were equal.

To illustrate the interaction between the current and interface, close-up snapshots of this experiment at late times are shown in figure 3.5. These show that the turbulence behind the head of the gravity current is partially suppressed as the thickness of the lower-layer ambient about the head thins. After the gravity current penetrates through the lower-layer, the head is surrounded by a uniform ambient of density ρ_2 and larger turbulent fluctuations are again observed. This same phenomenon was seen in all supercritical cases in which the two-layer ambient interface intersected the slope and the gravity current front penetrated into the upper layer. The observations suggest that the close proximity of a density interface can suppress mixing and entrainment into the current head.

An example of a critical experiment, for which the current and disturbance speed are comparable, is shown in figure 3.6. In the snapshot shown in figure 3.6 a, the gravity current head is surrounded by lower-layer fluid far along its length, as compared to the supercritical current shown in figure 3.4 a. The time-series of the gravity current height in figure 3.6 b exhibits similar features

a) Snapshot of a critical gravity current at t = 20 s

b) Gravity current height

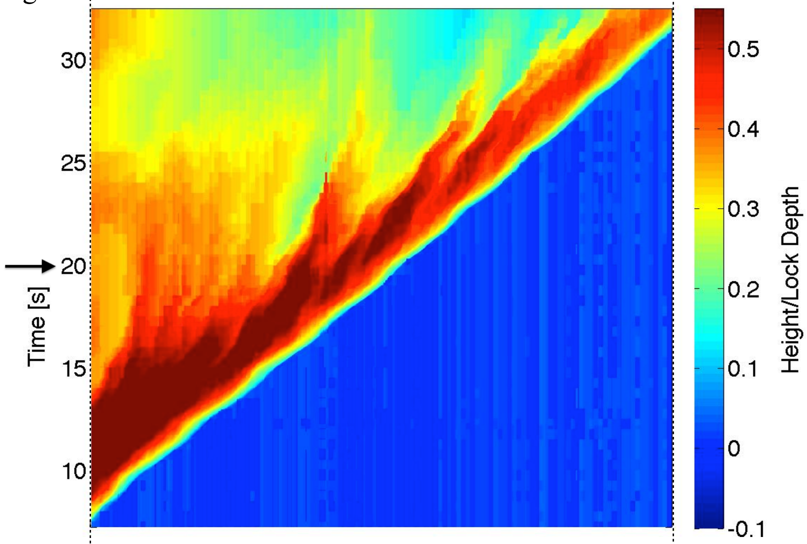

c) Interface displacement

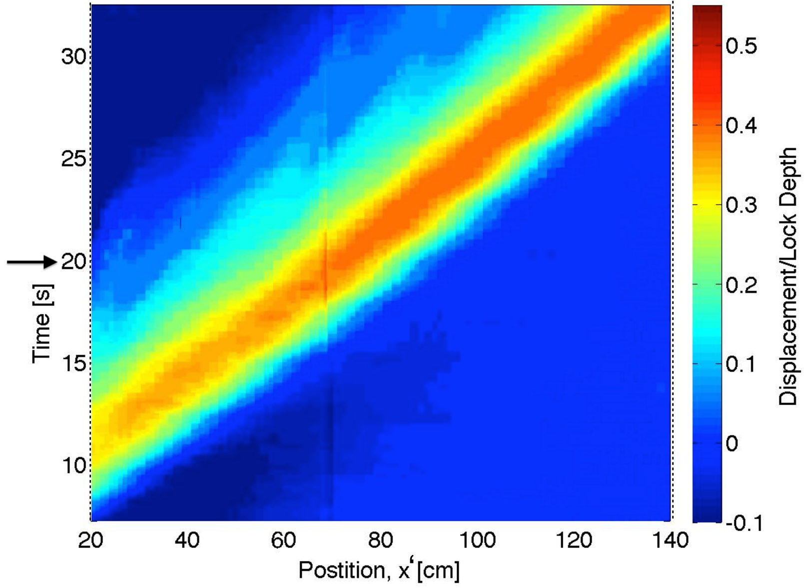

Figure 3.6: [Color] As in figure 3.4 but showing an example of a critical flow with $D/H = 0.33$, $s = 0.052$ ($\theta = 3°$), $\rho_0 = 1.0083\,\mathrm{g/cm^3}$, $\rho_1 = 1.0017\,\mathrm{g/cm^3}$, and $S = 0.34$.

to that of the supercritical current. In particular, the front advances at near-constant speed. Behind the head, however, dense fluid in the tail decelerates through a series of distinct pulses. In other experiments of critical gravity currents, a slight deceleration of the front and/or the formation of a secondary front was observed (features commonly observed for subcritical currents, as discussed in more detail below). Like the supercritical case, the interfacial disturbance, shown in figure 3.6 c is again seen to maintain a near-constant speed, amplitude, and width. But in this case the gravity current does not overtake the interfacial disturbance.

Figure 3.7 shows the results from a subcritical gravity current experiment, for which the gravity current speed was less than the interfacial disturbance speed. In the snapshot taken 20 s after release, shown in figure 3.7 a, the gravity current has a thin front at $x' \simeq 80\,\mathrm{cm}$ and a trailing bulge at $x' \simeq 50\,\mathrm{cm}$. These features differ qualitatively from those of supercritical gravity currents which exhibit the more familiar raised head with turbulent structures in the lee. The evolution of the thin front and trailing bulge can be tracked in figure 3.7 b. The gravity current head had a maximum nondimensional height of 0.40, at $x' = 20\,\mathrm{cm}$, $t = 10\,\mathrm{s}$ after release from the lock. Thereafter it propagated at near-constant speed, but the head height decreased rapidly until the front abruptly halted. After the front came to rest, the fluid inside the head continued to drain downslope, thus preventing the front from continuing its upslope propagation. While the primary head propagated upslope, a second head developed downstream with a maximum nondimensional height of $d/D \simeq 0.45$ at $t = 16\,\mathrm{s}$. This secondary head also propagated rightward at near-constant speed while the head-height rapidly decreased until the secondary front halted. Figure 3.7 c shows that the interfacial displacement likewise formed a distur-

a) Snapshot of a subcritical gravity current at t = 20s

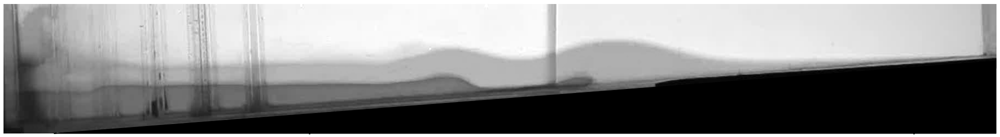

b) Gravity current height

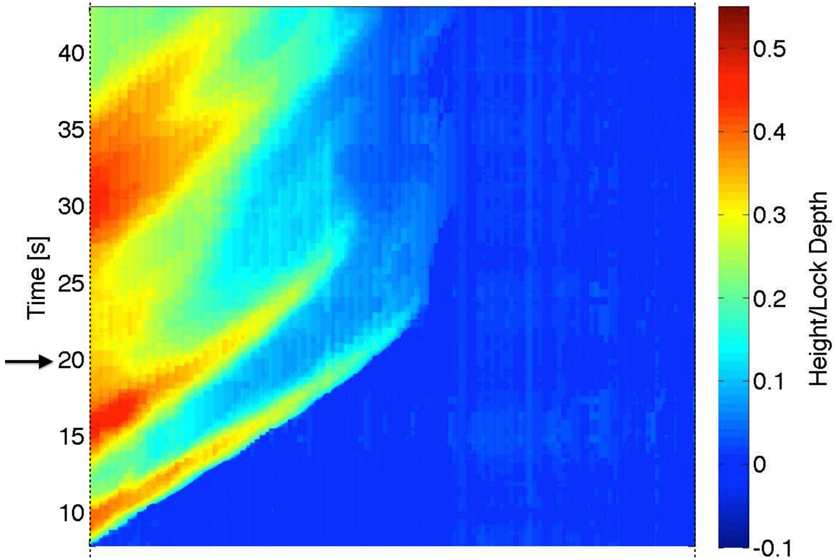

c) Interface displacement

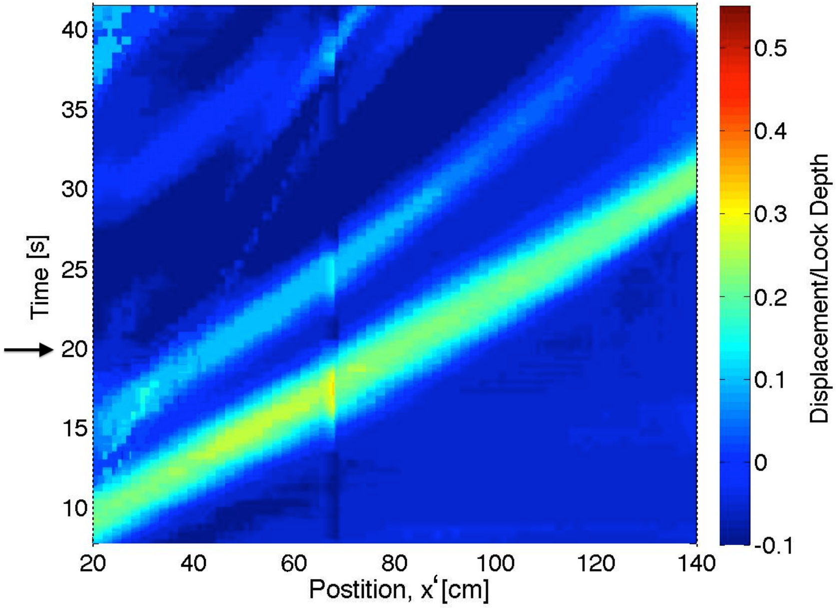

Figure 3.7: [Color] As in figure 3.4 but showing an example of a subcritical flow with $D/H = 0.33$, $s = 0.052$ ($\theta = 3^\circ$), $\rho_0 = 1.014\,\mathrm{g/cm^3}$, $\rho_1 = 1.008\,\mathrm{g/cm^3}$, and $S = 062$.

a) $t = 21\,\mathrm{s}$

b) $t = 27\,\mathrm{s}$

c) $t = 33\,\mathrm{s}$

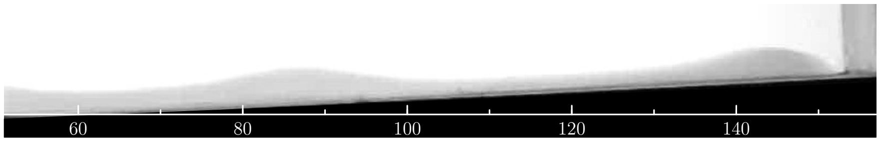

Figure 3.8: Close-up snapshots of the subcritical gravity current experiment shown in figure 3.7 focusing on the shoaling interfacial disturbance at times (a) $t = 21\,\mathrm{s}$, (b) $t = 27\,\mathrm{s}$, and (c) $t = 33\,\mathrm{s}$. The field-of-view shows a portion of the tank close to the right end wall; the scale below panel c indicates the horizontal position from the lock-gate in cm.

bance that surrounded the leading gravity current head but which continued to propagate at constant speed even after the leading front of the current stopped. A trailing interfacial disturbance also developed surrounding the secondary gravity current head. This too travelled at near-constant speed to the end of the tank even after the secondary front halted. The secondary gravity current head and secondary interfacial disturbance were present in most subcritical gravity current experiments and also some of the critical experiments. The observed sudden halting of the current front and steady advance of the interfacial disturbance was typical of subcritical gravity current experiments. These observations are also consistent with observations of experiments of horizontally propagating gravity currents and intrusions in stratified fluid (Maxworthy *et al.* (2002); Rottman & Simpson (1983); Sutherland *et al.* (2004); Mehta *et al.* (2002); Munroe *et al.* (2009)). Hence the bottom slope in our experiments is not expected to play a significant role in the formation of leading and secondary fronts and their sudden stop during subcritical experiments.

However, the slope does play a role in the consequent evolution of the interfacial disturbance which, after leaving the gravity current behind, continued to propagate rightward as a shoaling internal solitary wave. As the lower layer shallowed to zero depth, the wave transformed into a gravity current all the while maintaining its speed, as shown in figure 3.8. Of course at longer times, this newly developed gravity current also gradually decelerated and stopped.

Whether the gravity current was classified as supercritical, critical, or subcritical, the initial front speed, U_{GC}, was found from the slope of the least-squares best-fit line through data of the front position *vs* time over the range $0.5L_\ell < x' < L_\ell$. This was measured in the x'-direction, which is at an angle, $\theta = \tan^{-1}s$, to the ambient interface. This range was chosen to be the distance over which the current was well formed but not yet significantly influenced by the slope or interfacial disturbance. The initial front speed was found to vary by much less than the representative measurement error ($\pm 3\,\%$) and so could be approximated as constant at least as far as one lock-length away from the gate. The deceleration of the gravity current, $d_{x'}$, was set to be twice the coefficient of the t^2 term found from the least-squares best-fit quadratic that was fit to the front position *vs* time data. In most experiments the range of points used to compute $d_{x'}$ was $0.5L_\ell < x' < L - 0.5L_\ell$. However, in cases where the front was observed to come to an abrupt stop (e.g. as in the subcritical case shown in figure 3.7), $d_{x'}$ was determined up to the position where the front first stopped.

The amplitude, A, of the interfacial disturbance was found by averaging the maximum displacement of the interface over the range

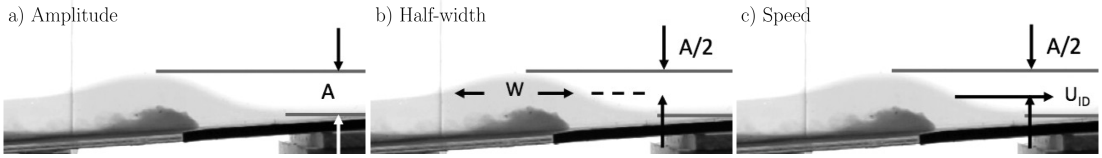
a) Amplitude
b) Half-width
c) Speed

Figure 3.9: Schematic of measurement methods for the interfacial disturbance amplitude (a), half-width (b), and speed (c).

$0.5L_\ell < x' < L - 0.5L_\ell$ as shown in figure 3.9 a. Beyond an initial transient stage, the interfacial disturbance was observed to have an amplitude that was constant within measurement error (±1 cm) as it propagated to the right end of the tank. The amplitude remained constant even in subcritical cases for which the current halted and the interfacial disturbance, now identified as a solitary wave, shoaled on the bottom slope so transformed itself into a gravity current. Of course, in those instances the measurement of wave amplitude, A, became interpreted as a measurement of gravity current head height after shoaling occurred. The half-width, W, of the interfacial disturbance was found by measuring the distance between positions where the interfacial disturbance had half the maximum height (figure 3.9 b). Measurements of W were made during the time that both positions, one of which was to the left of the maximum, the other to the right, were within the range $0.5L_\ell < x' < L - 0.5L_\ell$. The speed, U_{ID}, of the interfacial disturbance was determined by tracking the position of the half-amplitude displacement ahead of the crest (figure 3.9 c). This was found to be a good approximation of the speed of the entire interfacial disturbance, which was observed to undergo little dispersion (e.g. see figures 3.4 c, 3.6 c, and 3.7 c).

For both the uniform ambient experiments and the two-layer stratified ambient experiments, effort was taken to eliminate or reduce the errors throughout the process of setting up, conducting, and analyzing the experiments. Inevitably, some errors could not be eliminated. Measurement or analysis errors could have been caused by non-uniform density throughout an ambient layer or a visually obscured interface prior to or during the experiment execution. A non-uniform density would cause an inaccurate density measurement and thereby cause an error of g'. The obscured interface could cause measurement errors in the lock-fluid depth or lower-layer ambient depth prior to the execution of the experiment. During the experiment, the obscured interface could cause analysis errors of the gravity current height or position and/or the interfacial disturbance position and shape. These errors may be the reason that particular data points shown in any of the figures in Chapter 4 are incongruent with the majority of data points shown in the same figure.

Chapter 4

Results

The experimental results are compared with theory and presented below. Results of the uniform ambient experiments, in §4.1, include the gravity current front speed along the horizontal portion of the tank, the deceleration of the gravity current along the slope, and analysis of the gravity current head shape. Both the results and discussion of §4.1 have been previously published (Marleau *et al.* (2014)). The two-layer stratified ambient experimental results, presented in §4.2, include analysis of the initial gravity current speed, the along-slope deceleration and stopping distance of the gravity current, and properties of the interfacial disturbance.

4.1 Uniform Ambient Experiments

4.1.1 Gravity Current Horizontal Front Speed

Consistent with related experimental studies (Shin *et al.* (2004); Rottman & Simpson (1983)) and numerical studies (Härtel *et al.* (1999)) of bottom-propagating gravity currents on horizontal surfaces, the gravity current front attained a constant speed within 1 s after removal of the gate and it maintained that speed until reaching the base of the slope (e.g. see figure 3.2 d). For all uniform ambient experiments, the front speed, U_{GC}, was measured and the corresponding Froude number, Fr, was calculated using (2.1) with the reference density chosen as $\rho_{00} = \rho_2$. This was compared to existing theoretical and experimental values. The Froude numbers of the full-depth lock-release experiments had an average value of $\mathrm{Fr} = 0.45 \pm 0.02$. This was slightly smaller than the value predicted by Benjamin (1968) but was consistent with other experimental findings (Shin *et al.* (2004); Huppert (1982); Simpson (1972)). The Froude numbers for the $D/H = 3/4$ and $D/H = 1/2$ experiments had average values of $\mathrm{Fr} = 0.46 \pm 0.03$ and 0.40 ± 0.04, respectively. These results are also consistent, within error, with the measurements made by Shin *et al.* (2004), who found $\mathrm{Fr} = 0.48$ and 0.44, respectively, and , moreover, show reasonable agreement with the predictions given by (2.2) of $\mathrm{Fr} = 0.48$ and 0.43, respectively. For both full- and partial-depth lock-release experiments, energy loss due to mixing is believed to be the reason that the experimental results are overpredicted by theory.

4.1.2 Front Deceleration Along the Slope

In all experiments the gravity current front slowed down immediately upon reaching the slope. This was most obvious in cases with larger values of s and g'. Furthermore, between first encountering the slope and finally coming to rest, the deceleration of the front was nearly uniform. As shown in figure 4.1, the measured deceleration scales with g', s, and D/H in a way that is consistent with the theoretical prediction given by (2.5). No systematic deviation from this prediction was found in experiments with different s. A comparison of the experimental results and the prediction of (2.7) is not illustrated because (2.5) demonstrated better agreement with the experimental results. The dashed line of figure 4.1 is the least-squares best-fit line of the entire data set and has a slope of

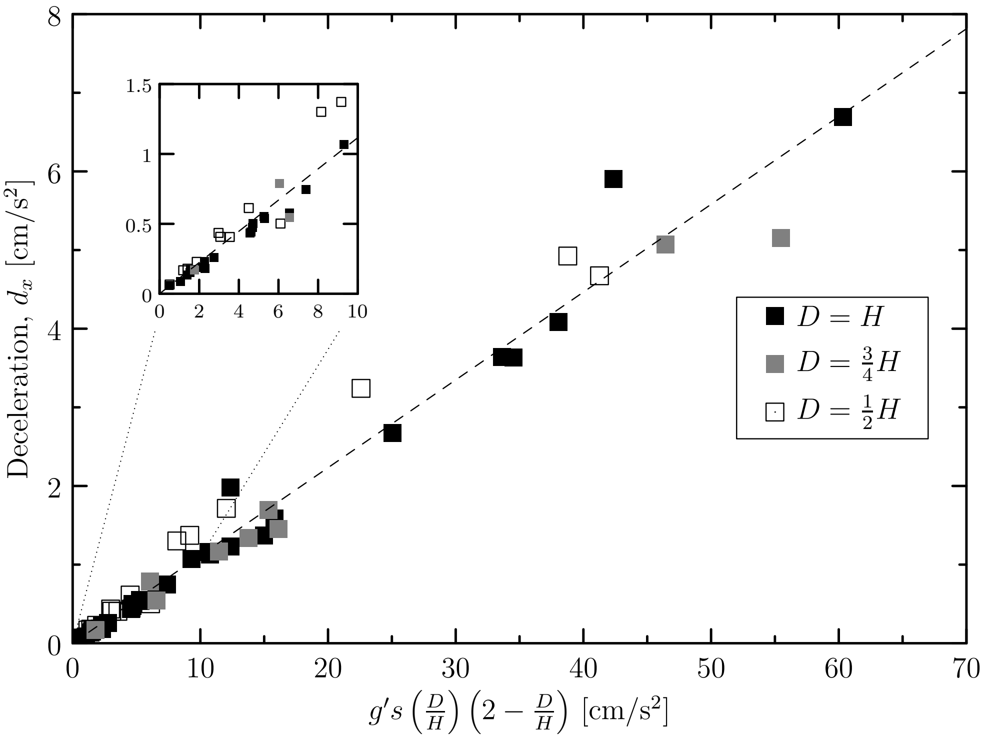

Figure 4.1: Deceleration of the gravity current head found from a multitude of experiments that varied the slope, s, from 0.24 to 1.14 and the reduced gravity, g', from $2\,\mathrm{g/cm^3}$ to $73\,\mathrm{g/cm^3}$. The dashed line is a least-squares line of best-fit. The error of each data point is approximately equal to the size of the markers in the main figure.

0.112 ± 0.002 leading to the following empirical relationship for the rate of deceleration of the gravity current front:

$$d_x = (0.112 \pm 0.002)\; g's\left(\frac{D}{H}\right)\left(2 - \frac{D}{H}\right). \tag{4.1}$$

The numerical prefactor shows robust agreement with the predicted value of 1/8, which is remarkable considering the relative simplicity of the theory outlined in Chapter 2.

4.1.3 Gravity Current Head Shape

Figure 4.2 depicts the evolution of the gravity current shape during upslope propagation for five different experiments. The snapshot

a) $D/H = 1 \quad s = 0.25 \quad g'_{02} = 22\ \mathrm{g/cm^2}$

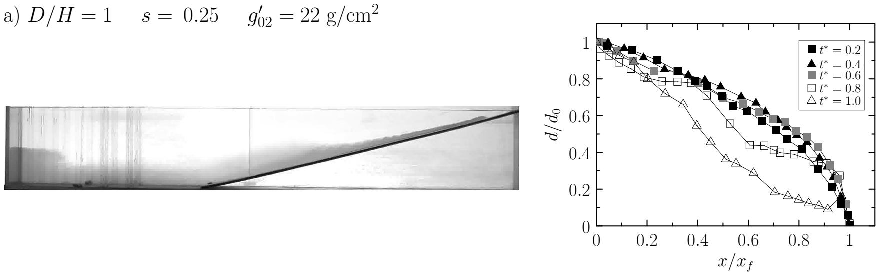

b) $D/H = 1 \quad s = 0.25 \quad g'_{02} = 44\ \mathrm{g/cm^2}$

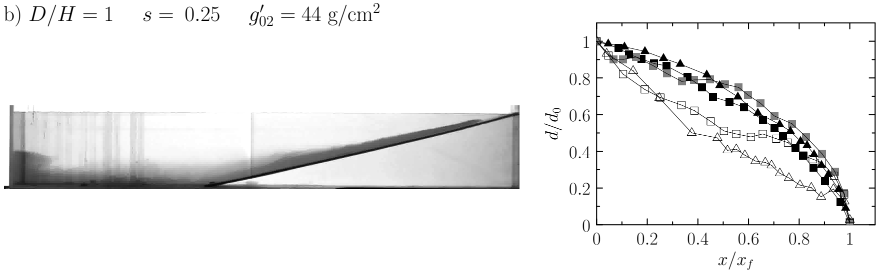

c) $D/H = 1 \quad s = 0.58 \quad g'_{02} = 44\ \mathrm{g/cm^2}$

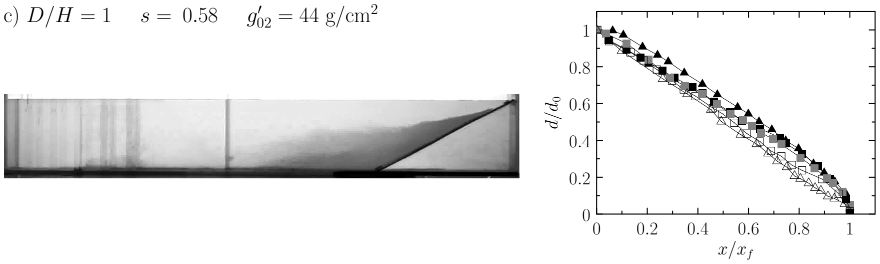

d) $D/H = 1 \quad s = 1.1 \quad g'_{02} = 52\ \mathrm{g/cm^2}$

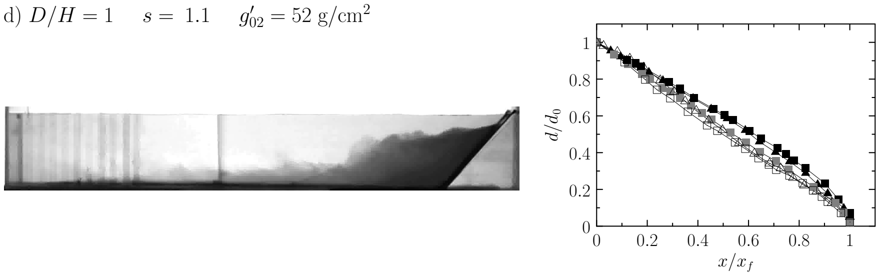

e) $D/H = \frac{1}{2} \quad s = 1.1 \quad g'_{02} : 44\ \mathrm{g/cm^2}$

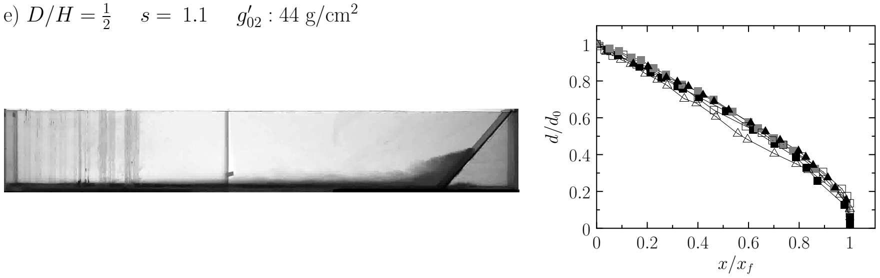

Figure 4.2: Comparison of gravity current shapes in five different experiments with indicated D/H, s, and g'. Snapshots (left) show gravity currents at the instant the front has reached its maximum upslope elevation. Plots of nondimensional height *vs* nondimensional horizontal position (right) are given at five different times ($t^* = 0.2, 0.4, 0.6, 0.8, 1.0$) as indicated by the legend in the top-right plot.

image on the left side of each panel shows the gravity current at its maximum upslope position. In each case it can be seen that the gravity current fluid attains a height slightly different than D, its initial height inside the lock. From many experiments, it was found that the gravity current fronts reached average heights of $0.86D$, $0.99D$, and $1.15D$ for cases with D/H =1, 0.75, and 0.5, respectively. Moreover, the gravity current shape is much thinner and more elongated on the shallower slopes as compared to the thicker gravity currents observed on steep slopes. The plots shown on the right side of each panel in figure 4.2 depict the nondimensional gravity current height versus the nondimensional horizontal position at various nondimensional times, t^*, where $t^* = t/t_{\text{max}}$. The overlap of the rescaled gravity current shapes indicates that the gravity current maintains a nearly self-similar shape during much of its upslope propagation. Specifically, in all cases shown, the decrease of the nondimensionalized head height was linear between the start of the slope and up to approximately 80% of the distance to the nose and up until $t^* = 0.8$. The self-similarity was most prominent when the slope is steep (figure 4.2 c, d, e) in which case the deceleration time was brief and little fluid flowed downslope prior to the front reversing direction from upslope to downslope flow. Conversely, in experiments with a shallow slope (figure 4.2 a, b), the front took a longer time to decelerate, in which case a larger volume of dense fluid from behind the front reversed direction and flowed downslope before the front reached its maximum height. This downslope flow increased the value of $d_0(t)$, resulting in smaller values of d/d_0 and a deviation from the self-similar shape evident at earlier times or for larger values of s.

4.2 Two-Layer Stratified Ambient Experiments

4.2.1 Gravity Current Upslope Front Speed

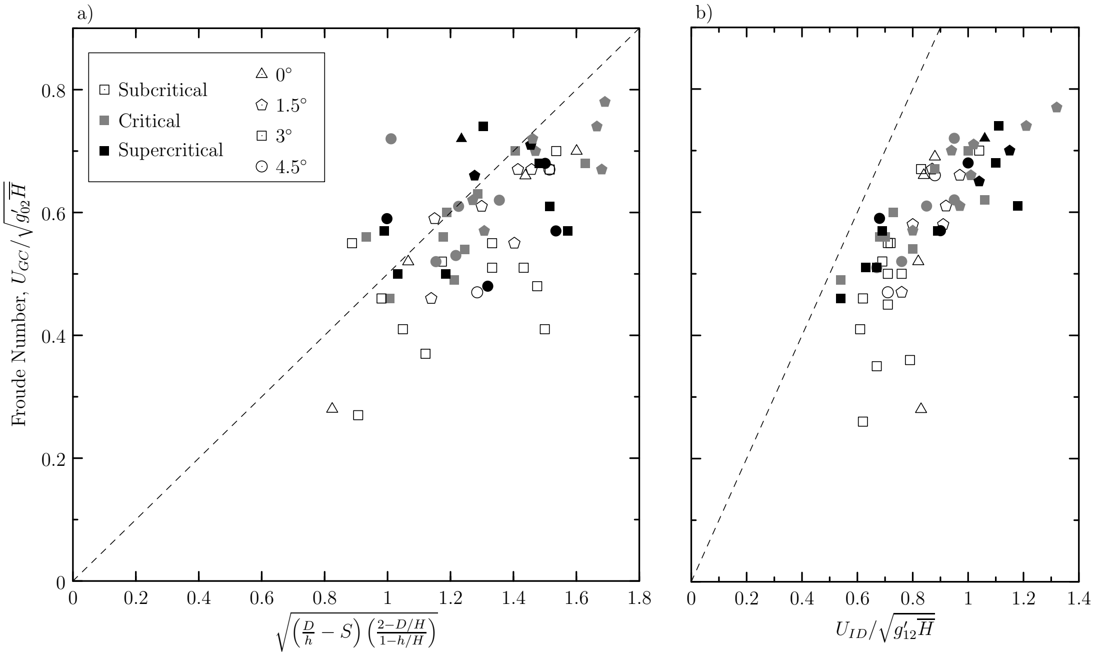

Figure 4.3: (a) Measured Froude number *vs* the geometric parameter given by (2.8). The dashed line has slope 1/2. (b) Measured Froude number *vs* the nondimensionalized interfacial disturbance speed. The dashed line has unit slope. Measurement errors are approximately equal to the size of the symbols.

The gravity current front was found to propagate at a nearly constant speed at early times after the initial collapse of the dense lock-fluid; the bottom slope did not have an appreciable affect on the gravity current front speed within the first lock-length. Figure 4.3 a shows the measured relative speed compared to the theoretical prediction (2.8). As defined previously, $\overline{H} = (H-h)h/H$ where H and h are the ambient layer heights measured at the gate. The least-squares best-fit line through the data has a slope of (0.444 ± 0.009) which is moderately smaller than the predicted slope of $1/2$. However, this result is close to the prefactor of 0.45 found in similar gravity current experiments (Shin *et al.* (2004); Sutherland *et al.*

(2004)) and in the uniform ambient upslope case, as described in section 4.1. If one considers only critical and supercritical flows, the least-squares best-fit line has a slope of 0.464 ± 0.012. In other words, subcritical gravity currents deviate most from the relationship prescribed by (2.8) presumably as a consequence of imparting more momentum to interfacial disturbances during their formation, a loss not accounted for in the theory used to derive (2.8). Figure 4.3 b compares the gravity current front speed, U_{GC}, and the interfacial disturbance speed, U_{ID}. The speeds, U_{GC} and U_{ID}, are nondimensionalized using different scaling parameters. In particular, U_{ID} is scaled by the shallow water speed, $\sqrt{g'_{12}}$ in which $g'_{12} = (\rho_1 - \rho_2)/\rho_2$ and $\overline{H}$ is as defined above. Therefore, data for subcritical, critical, and supercritical gravity currents are interspersed amongst each other in this plot. Because the dashed line in figure 4.3 b has unit slope, it is clear that the nondimensional gravity current front speed is always less than the nondimensional interfacial disturbance speed. Whether the gravity current actually travelled faster or slower than the interfacial disturbance depended, of course, on whether the flow was supercritical ($U_{GC} > 1.04 U_{ID}$) or subcritical ($U_{GC} < 0.96 U_{ID}$) respectively. A best-fit line through the data of figure 4.3 b (not shown) has a slope of 0.673 ± 0.013, suggesting an approximate empirical relationship

$$U_{ID} \simeq (1.49 \pm 0.03)\sqrt{S}\, U_{GC}. \tag{4.2}$$

Baines (1984) developed a regime diagram for the qualitative behaviour of a two-layer flow over a streamlined obstacle. Rottman & Simpson (1989) adapted this analysis by substituting the solid obstacle with a gravity current of non-constant shape propagating over a horizontal boundary, beneath a two-layered stratified ambient. Rottman & Simpson's curves are duplicated in figure 4.4, which also includes data points corresponding to the present experiments. All the gravity currents studied here fall within the regime in which the interfacial disturbance above the crest of the gravity current is expected to exhibit upstream and downstream asymmetry (see figure 2 of Rottman & Simpson (1989)). Consistent with this prediction, asymmetry of the interfacial disturbance was observed in each of our experimental runs. However, it was unclear whether the asymmetry was a due to interactions between the gravity current and interface or instead due to the sloped bottom.

With some exceptions, the gravity current tended to be supercritical both at low values of $D/2h$ and at high values of $U_{GC}/\sqrt{g'_{12}h}$. Conversely, the gravity current tended to be subcritical both at high values of $D/2h$ and at low values of $U_{GC}/\sqrt{g'_{12}h}$. The general trend of increasing stratification parameter S from the top-left to the bottom-right of each panel of figure 4.4 is analogous to the trend noted by Rottman & Simpson (1989), who measured stratification by a parameter $\alpha \equiv (\rho_0 - \rho_1)/(\rho_1 - \rho_2)$, which increased from the bottom-right to the top-left of their regime diagram images.

4.2.2 Supercritical Gravity Current Deceleration

Over the length of the tank the deceleration, $d_{x'}$, of supercritical gravity currents was found to be approximately constant even as the current propagated from the lower to the upper layer, as shown in figures 3.4 and 3.5. A similar observation was made for the uniform ambient case. In figure 4.5 the prediction given by (2.12) is compared with the measured deceleration determined both from the two-layer ambient data and the uniform ambient data. It can be seen that supercritical gravity currents decelerate in a similar manner to the relationship found for the uniform case. In the case of a uniform ambient $\overline{g}' = g'_{02}$ and $S = 0$ making the axes of figure

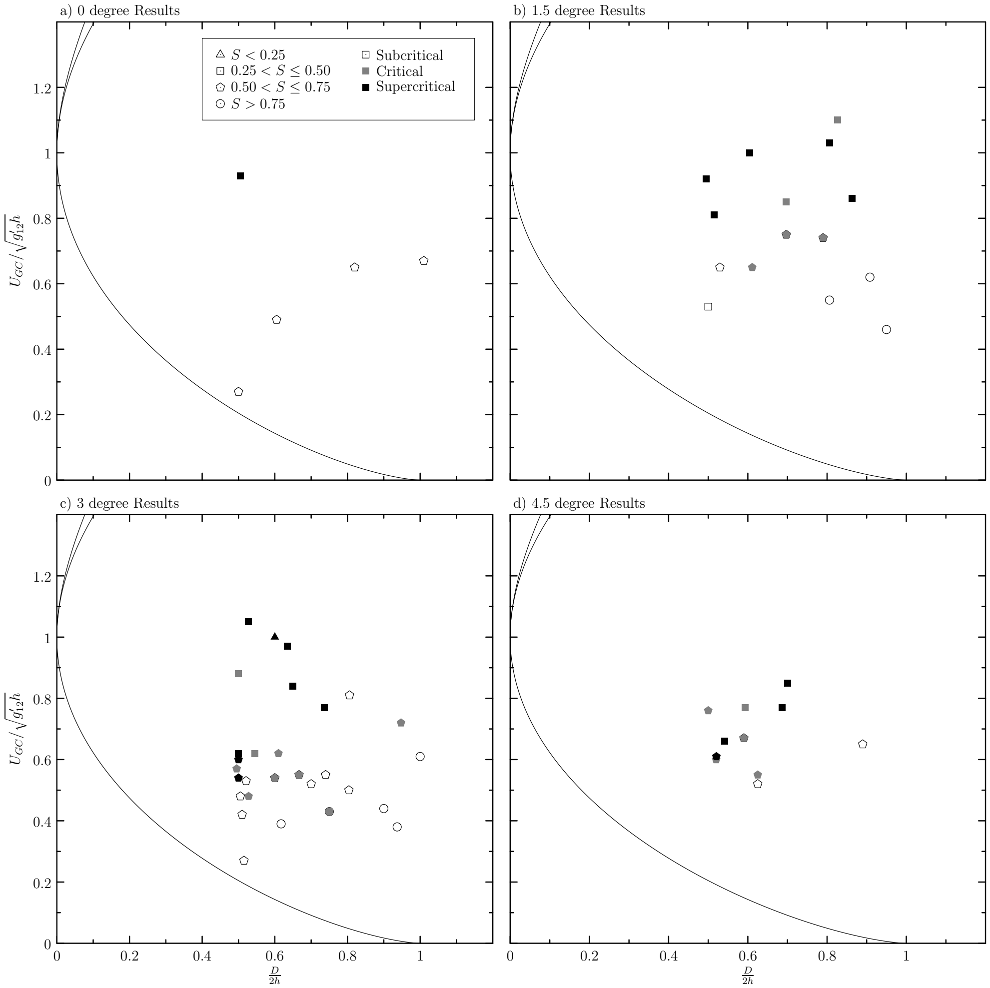

Figure 4.4: Nondimensionalized front speed *vs* the geometric parameter $D/2h$. The axes are identical to those in figure 9 of Rottman & Simpson (1989) as are the curves showing the largest possible value of $D/2h$ associated with a symmetric solution of the shallow water equations for a given Froude number. Values of the stratification parameter, S, are represented by the shape of the symbol. The relative speeds of the gravity current and interfacial disturbance are represented by the shade of the symbol. These conventions are indicated in the legend in panel a.

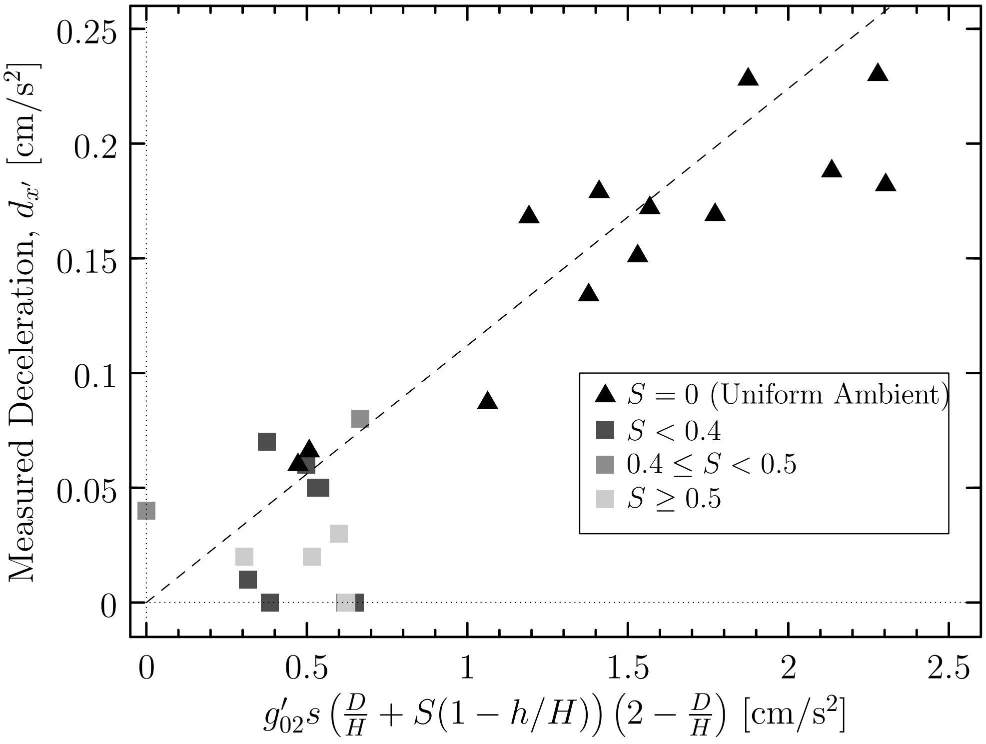

Figure 4.5: Front deceleration for the supercritical gravity current experiments in two-layer fluids (squares) and in uniform density fluid (triangles). In the former case, the shade of the square specifies the stratification parameter, S, which ranged between 0.24 and 0.64. The dashed line represents the relationship found for the uniform ambient case and has a slope of 0.112. Measurement errors are smaller than the size of the symbols.

4.5 equivalent to those of figure 4.1. The stratification parameter, S, does not appear to have an effect on the rate of deceleration within the supercritical regime. In particular, the $S = 0$ uniform ambient data shows a similar trend to the data with S value ranging up to 0.64. If the deceleration was allowed to vary with time as predicted from twice differentiating (2.11), the magnitude of the deceleration would, for the experimental parameters given above, be predicted to increase by an average value of $0.02\,\mathrm{cm/s^2}$ over the length of the tank. This change is the same order of magnitude as the measurement error thereby validating the constant deceleration assumption. The deceleration of a critical or a subcritical gravity current is poorly predicted by (2.12) because of significant interactions with the interface that, in some cases, bring the front to an abrupt halt – see figure 3.7 and the discussion of the next subsection.

4.2.3 Gravity Current Stopping Distance

In some experiments the deceleration of the gravity current front resulted in the gravity current stopping before reaching the right end wall of the tank. Figure 4.6 compares the measured stopping distance of the front with the prediction given in (2.14). Recall that the analytical solution was derived under the assumption that the leading order deceleration effects are produced by the decreasing ambient depth (in the same manner as the deceleration prediction given by (2.12)). Gravity currents halted at a shorter distance for one of two reasons. In the majority of subcritical cases, the interfacial disturbance extracted momentum as it overtook the front and continued traveling in the downstream direction as the current head decelerated to a halt (e.g. see figure 3.7). In other cases, as the gravity current propagated upslope, fluid continually drained from the gravity current head and flowed back downslope. Eventually the draining completely depleted the volume of the head. The gravity currents that stopped due to interaction with the interface were found to stop before the distance predicted by (2.14). Gravity currents that stopped due to mass depletion tended to stop at a distance greater then that predicted by (2.14).

4.2.4 Interfacial Disturbance Properties

Figure 4.7 compares the semi-empirical equation developed by Tan *et al.* (2010) against laboratory measurements of the maximum in-

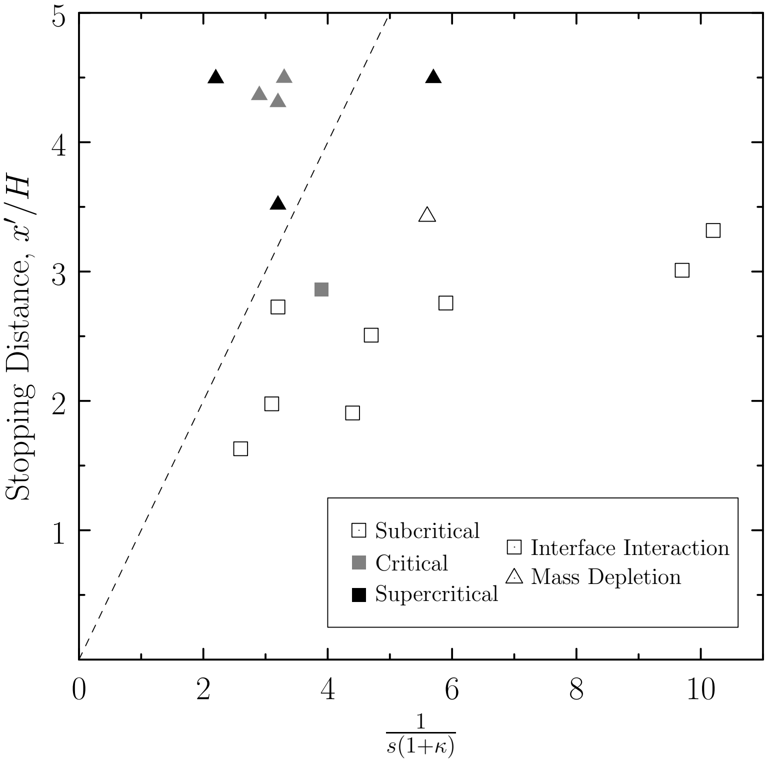

Figure 4.6: Measured *vs* predicted stopping distance. The triangles represent experiments in which the gravity current propagation ceased due to fluid flowing back downslope thereby depleting the volume of the head. The squares represent experiments in which the gravity current front decelerated because of an interaction with the interfacial disturbance. Open, grey, and black symbols represent subcritical, critical, and supercritical gravity currents, respectively. Measurement errors are approximately half the size of the symbols.

terfacial displacement. Applying the semi-empirical result (2.17) to our measurements yields gives $\alpha = 0.67$, somewhat smaller than the Tan *et al.* (2010) result of $\alpha \simeq 0.87$.

In general, the interfacial disturbance was observed to travel faster for larger A, as shown in figure 4.8. This observation is consistent with Korteweg-de Vries (KdV) theory, which predicts that the speed of moderately large solitary waves increases linearly with amplitude. However, the relative amplitudes of the "waves" observed here were comparable to the lower ambient depth and were, therefore, much larger than those that can be well described by KdV

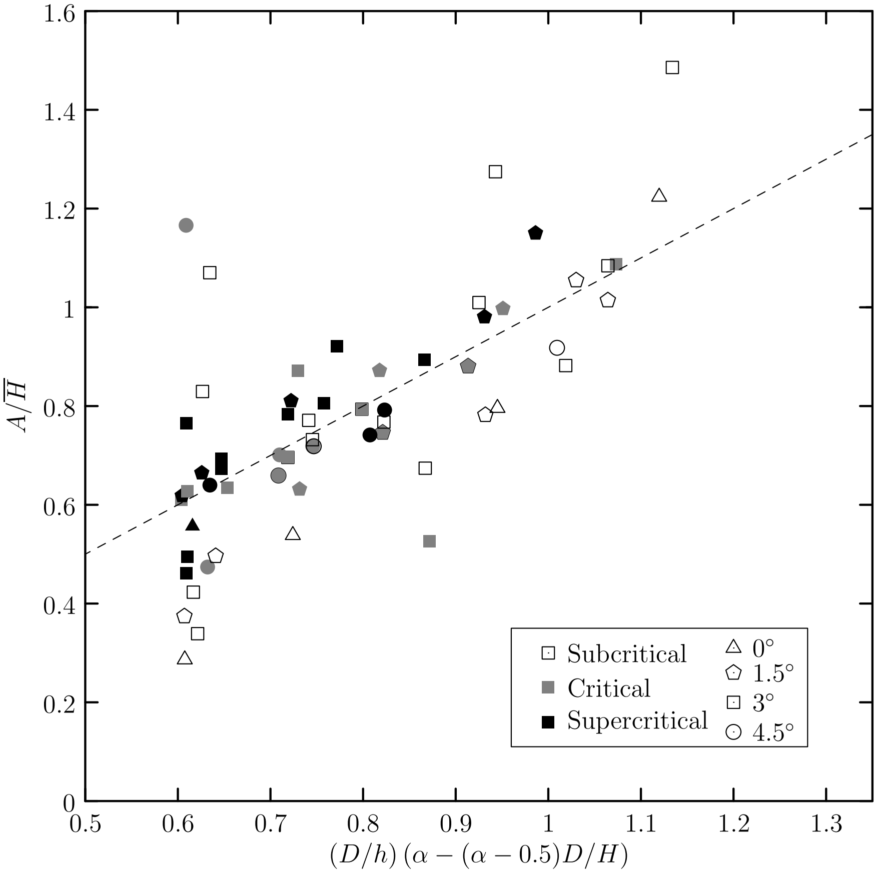

Figure 4.7: Interfacial disturbance amplitude *vs* the semi-empirical prediction (2.17) developed by Tan *et al.* (2010). The dotted line uses $\alpha = 0.67$ in (2.17) rather than $\alpha = 0.87$, the value suggested in this earlier study. Measurement errors are approximately equal to the size of the symbols.

theory (Grue *et al.* (1999)). Additionally, unlike solitary waves, the interfacial disturbance in most of our experiments had dense fluid associated with the gravity current beneath it. Figure 4.8 displays the speed of the interfacial disturbance is nondimensionalized by the shallow water speed at $x' = L/2$. More specifically $C_0 = \sqrt{g'_{12}\overline{H}_{\mathrm{mid}}}$ where $g'_{12} = g(\rho_1 - \rho_2)/\rho_1$ and $\overline{H}_{\mathrm{mid}} = (H-h)(2h-Ls)/(2H-Ls)$. The interfacial disturbance speed exceeded the shallow water speed in the majority of experiments, indicative of the disturbance being a nonlinear phenomenon. The relative speed of disturbances generated by subcritical gravity currents was generally larger than

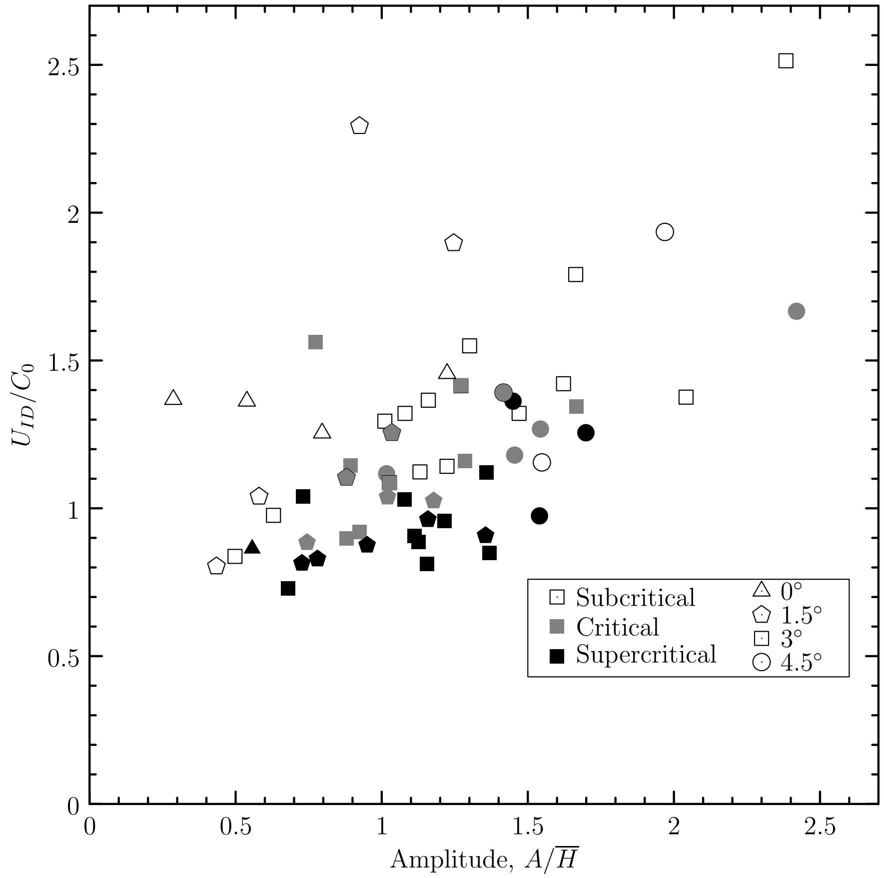

Figure 4.8: Interfacial disturbance speed *vs* interfacial disturbance amplitude. Measurement errors are approximately equal to the size of the symbols.

the relative speed of disturbances generated by supercritical gravity currents.

Figure 4.9 compares the half-width, W, of the interfacial disturbance to its amplitude, A. Unlike KdV theory, which predicts that W should decrease as A increases, figure 4.9 shows that the width increases approximately linearly with amplitude according to $W = (5.04 \pm 0.16)A$. The observation is consistent with previous experiments examining the properties of solitary waves at amplitudes $A > 0.5\overline{H}$, beyond the realm of KdV theory (Grue *et al.* (1999); Sutherland *et al.* (2013*a*)). In presenting data in figures 4.8 and 4.9, the intent is not to suggest causal relationships between distur-

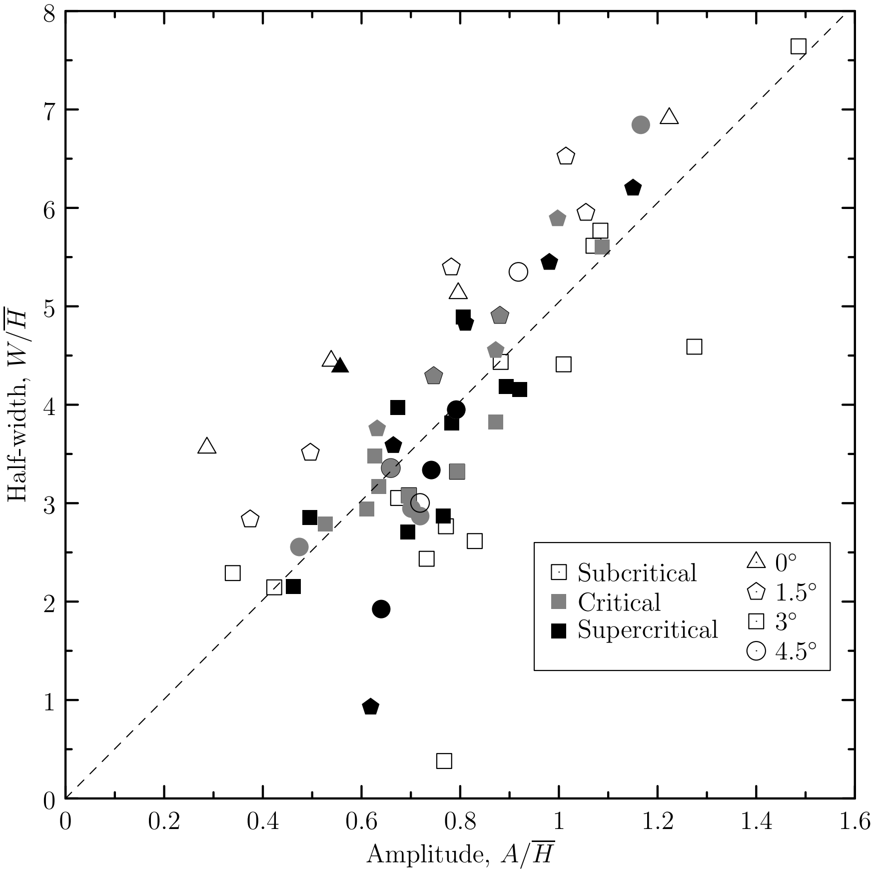

Figure 4.9: Half-width of the interfacial disturbance *vs* amplitude of the interfacial disturbance. The dotted line represents the least-squares best-fit. Measurement errors are approximately equal to the size of the symbols.

bance speed and width upon amplitude. Ultimately, all these factors are influenced by a combination of initial conditions. Generally, it is found that experiments with small (large) lock-depth, D, relative to $\overline{H}$ produced an interfacial disturbance having small (large) amplitude, small (large) width, and slow (fast) speed. However, their values were additionally influenced by the relative stratification and ambient layer depths. A detailed investigation of these properties lies beyond the scope of the present study.

Chapter 5

Summary and Conclusions

An examination of Boussinesq, high Reynolds number gravity currents propagating upslope was conducted through rectilinear full- and partial-depth lock-release experiments with various slopes lock-depths and relative densities of gravity currents in uniform and two-layer stratified ambients.

For the uniform ambient investigation, a WKB-like theory was developed as an extension of existing theory (Benjamin (1968); Shin *et al.* (2004); Sutherland *et al.* (2013*b*)) to determine a heuristic prediction for the along-slope deceleration of the gravity current. Consistent with this theory, it was found that the gravity current front propagated at a constant velocity along the horizontal portion of the tank and experienced near-constant deceleration as soon as it began propagating upslope. More quantitatively, the prediction for the horizontal component of deceleration was estimated to be $d_{x'} = g'_{02}s(D/H)\,(2 - D/H)\,/8$. The coefficient of 1/8 agrees well with the experimentally measured value of 0.112 ± 0.002. By comparison, Sutherland *et al.* (2013*b*) found that a full-depth lock-release surface gravity current propagating over a bottom slope decelerated as $d_{x'} = 0.31 g'_{02}s$. The magnitude of deceleration was larger in those experiments because the deceleration did not start until the nose was approximately halfway over the slope and, therefore, the front stopped over a shorter distance.

The shape analysis of the gravity currents within the uniform ambient revealed that the gravity current head steadily reduced in height as it propagated upslope. For steep slopes, the gravity current shape, scaled by the gravity current height at the base of the slope and the along-slope length, exhibited self-similar structure. For shallow slopes, this self-similarity was less robust.

Within the two-layer ambient investigation, gravity currents were classified as supercritical, critical, or subcritical depending upon whether their observed speed was respectively faster than, approximately equal to, or slower than the observed speed of the excited interfacial disturbance. In all cases, the prediction for the gravity current front speed, developed from an extension of the prediction of Shin *et al.* (2004), agreed well with observations. When nondimensionalized by the characteristic speed based on the lock-fluid density and upper ambient density, the gravity current speed was found to be comparable to, but less than, the interfacial disturbance speed normalized by the long wave speed of the two-layer ambient. Supercritical gravity currents were found to decelerate and stop in the same manner as upslope gravity currents in a uniform ambient. However, for all subcritical and some critical gravity currents the dynamics were qualitatively different; the front was found to stop rapidly as a consequence of interactions with the interfacial disturbance. Similar observations have been made previously for subcritical gravity currents in stratified ambients (Maxworthy *et al.* (2002); Mehta *et al.* (2002); Munroe *et al.* (2009)). The measured interfacial disturbance amplitude compared well to the prediction of Tan *et al.* (2010), but with a smaller fitting parameter. The half-width and speed of the interfacial disturbance were found to increase with amplitude and were generally larger in experiments with larger lock-depth.

Qualitatively, the evolution of the flow as the lower-layer depth decreased to zero were examined. In the case of subcritical gravity currents that came to rest, the interfacial disturbance was observed to transform into a solitary wave that continued its forward progression at a constant speed into progressively shallower lower-layer fluid. The shoaling wave then transformed into a gravity current all the while maintaining constant speed and amplitude. In cases of supercritical gravity currents, turbulence about the head was suppressed as the layer depth surrounding the head shallowed. After penetrating through the lower layer, the gravity current again adopted the structure of a turbulent gravity current, now propagating in the upper-layer ambient. In either case, the result was a gravity current propagating upslope in a uniform ambient.

The range of parameters explored here provides a starting point for understanding gravity currents propagating over complex topographies occurring in industry and in the environment. Future work will explore gravity currents propagating over nonuniform topography in uniform or stratified ambients to provide a model that more realistically captures coastal sea breezes interacting with atmospheric inversions.

Appendices

Appendix A

Uniform Ambient Experimental Data

Experiment Name	Slope, s	ρ0 [cm/s^2]	ρ2 [cm/s^2]	H [cm]	D [cm]	Maximum Distance Along-slope [cm]	U_GC [cm/s]	Deceleration [cm/s^2]
e130506a	1.15	0.9987	0.9966	30.1	15.3	18.3	2.8	0.23
e130513b	0.26	1.0011	0.9988	30.3	16.0	75.9	3.2	0.07
e130509a	0.56	1.0014	0.9986	29.9	15.8	35.1	3.4	0.17
e130307b	1.07	1.0001	0.9981	30.3	30.3	37.2	3.6	0.18
e130404a	0.24	1.0007	0.9983	30.3	30.3	114.5	3.7	0.06
e130405a	0.34	1.0013	0.9982	30.0	30.0	83.1	3.8	0.09
e130207a	0.72	1.0011	0.9982	30.1	30.1	43.4	4.0	0.19
e130404c	1.11	1.0015	0.9988	30.3	30.3	33.2	4.1	0.26
e130131a	0.56	1.0013	0.9982	30.5	30.5	52.5	4.2	0.17
e130920a	0.72	1.0050	0.9986	30.2	15.0	29.0	4.8	0.41
e130307a	0.34	1.0020	0.9984	30.1	30.1	87.9	4.8	0.13
e130920b	1.20	1.0054	0.9986	30.2	15.0	27.1	5.2	0.50
e130513a	0.25	1.0048	0.9989	30.2	15.2	80.4	5.4	0.18
e130509b	0.56	1.0049	0.9989	30.2	15.8	37.7	5.5	0.41
e130521a	0.59	1.0049	0.9984	30.0	15.1	36.0	5.7	0.44
e130404b	0.24	1.0057	0.9988	30.3	30.3	120.0	6.0	0.15
e130301b	1.09	1.0051	0.9983	30.0	30.0	34.5	6.1	0.58
e131105a	0.25	1.0052	0.9971	30.1	22.0	113.3	6.2	0.17
e130405b	0.34	1.0053	0.9986	30.0	30.0	86.1	6.2	0.23
e130207b	0.73	1.0054	0.9989	30.1	30.1	41.8	6.4	0.50
e130522a	0.57	1.0062	0.9984	30.1	30.1	51.7	6.6	0.44
e130131b	0.57	1.0065	0.9988	30.5	30.5	52.9	6.7	0.43
e130521b	0.55	1.0189	0.9989	30.1	15.0	30.3	8.8	1.30
e130124a	0.35	1.0113	0.9982	30.6	30.6	85.2	9.8	0.48
e130514a	0.25	1.0204	0.9943	30.2	15.2	80.7	10.0	0.61
e130131e	0.56	1.0200	1.0030	30.6	30.6	51.8	10.4	1.07
e130507a	0.57	1.0278	0.9991	30.5	14.2	31.3	10.4	1.72
e131105d	0.54	1.0205	0.9976	30.2	22.3	49.4	10.7	1.17
e130418a	0.67	1.0230	0.9979	30.1	15.0	30.7	10.9	1.98
e130131c	0.55	1.0198	1.0001	30.7	30.7	53.8	10.9	1.13
e130522b	0.56	1.0204	0.9973	30.2	30.2	50.1	10.9	1.23
e131105b	0.24	1.0204	0.9990	30.0	22.5	101.4	11.0	0.54
e130124b	0.35	1.0206	0.9997	30.6	30.6	81.3	11.0	0.74
e131105c	0.32	1.0192	0.9994	30.3	22.3	78.7	11.1	0.79
e130207c	0.72	1.0200	0.9998	30.1	30.1	41.4	11.4	1.58
e130117a	0.25	1.0210	0.9982	30.9	30.9	118.7	11.4	0.55
e131105e	0.55	1.0290	1.0002	30.4	21.9	45.4	12.3	1.70
e130118a	0.25	1.0208	0.9982	30.4	30.4	120.3	12.7	0.54
e130506b	1.13	1.0440	0.9983	30.1	15.1	18.5	13.4	4.67
e131121b	0.34	1.0360	1.0006	30.0	22.2	71.6	13.8	1.34
e130429a	1.10	1.0430	0.9986	30.0	14.2	19.7	14.1	4.92
e131121a	0.35	1.0408	0.9905	30.0	22.4	72.1	14.3	1.45
e130513c	0.25	1.0425	0.9981	30.3	15.2	83.3	15.1	1.37
e130124c	0.34	1.0489	1.0038	30.6	30.6	88.5	15.6	1.37
e130509c	0.56	1.0496	0.9975	30.0	15.4	38.1	15.6	3.24
e130118b	0.25	1.0467	1.0019	30.5	30.5	120.2	15.8	1.16
e130131d	0.58	1.0483	1.0036	30.7	30.7	51.8	16.7	2.67
e131127b	0.73	1.0588	0.9996	30.7	22.5	36.5	17.0	5.07
e130207d	0.73	1.0482	1.0037	30.1	30.1	41.5	17.3	3.64
e130430a	0.72	1.0490	0.9957	30.2	30.2	42.6	17.4	3.63
e130502a	0.70	1.0560	0.9983	30.4	30.4	41.2	17.9	4.09
e131127a	0.74	1.0623	0.9890	30.6	22.5	35.2	18.5	5.15
e130405d	1.14	1.0522	0.9997	29.9	29.9	30.5	19.7	6.70
e130430b	0.71	1.0662	1.0030	30.4	30.4	41.6	21.9	5.90

Table A.1: Uniform ambient data

Appendix B

Two-Layer Stratifient Ambient Experimental Data

Experiment Name	H_bar [cm]	D [cm]	Slope, s	ρ_0 [g/cm^3]	ρ_1 [g/cm^3]	ρ_2 [g/cm^3]	S	Fr (Hbar)	Stopping Dist [cm]	Acceleration [cm/s^2]	U_GC/U_ID	U_ID/C_0	W/H	A/H
e140716c	6.84	10.5	0.19	1.0136	1.0096	0.9986	0.73	0.28		-0.15	0.398	0.67	4.35	0.29
e140312a	6.67	10.3	0.18	1.0041	1.0024	0.9985	0.70	0.26	48.9	-0.13	0.503	0.50	3.14	0.83
e140224a	6.67	12.5	0.22	1.0031	1.0015	0.9985	0.66	0.36	57.2	-0.13	0.566	0.64	2.92	0.73
e140723b	6.60	15.8	0.28	1.0105	1.0086	0.9986	0.84	0.61		-0.09	0.727	0.75	6.43	0.78
e140212a	6.76	10.3	0.18	1.0151	1.0071	0.9986	0.51	0.35	76.5	-0.20	0.730	0.55	2.74	0.34
e140224c	6.67	18.0	0.32	1.0025	1.0015	0.9985	0.76	0.45	82.7	-0.07	0.734	0.58	5.32	0.88
e140716a	6.67	12.1	0.21	1.0081	1.0056	0.9985	0.74	0.52		-0.10	0.739	0.67	5.33	0.54
e140723d	6.66	19.0	0.34	1.0105	1.0099	0.9998	0.94	0.58	90.0	-0.04	0.752	0.65	7.84	1.01
e140314b	6.69	12.1	0.21	1.0043	1.0030	0.9985	0.77	0.41	61.1	-0.06	0.759	0.51	3.26	0.77
e140507a	6.75	16.4	0.29	1.0071	1.0043	0.9987	0.68	0.50		0.08	0.810	0.62	5.32	1.01
e140723c	6.60	17.8	0.32	1.0116	1.0090	0.9985	0.80	0.67		0.07	0.862	0.72	7.09	1.05
e140404a	6.33	18.0	0.32	1.0127	1.0106	0.9985	0.85	0.67		0.14	0.883	0.69	8.85	1.49
e140326a	6.64	14.0	0.25	1.0041	1.0020	0.9985	0.63	0.50	102.1	-0.01	0.888	0.58	0.46	0.77
e140721b	6.71	10.8	0.19	1.0104	1.0048	0.9986	0.528	0.58		-0.06	0.890	0.74	4.26	0.50
e140729c	6.81	10.5	0.19	1.0098	1.0041	0.9985	0.490	0.47	99.2	-0.09	0.896	0.61	3.47	0.37
e140514c	6.72	12.5	0.22	1.0044	1.0015	0.9979	0.55	0.47		0.01	0.901	0.58	3.58	0.72
e140224d	6.48	10.0	0.18	1.0033	1.0017	0.9976	0.72	0.55		0.04	0.909	0.59	6.68	1.07
e140731c	6.67	17.8	0.32	1.0071	1.0044	0.9984	0.693	0.66		0.04	0.912	0.72	6.42	0.92
e140716b	6.61	20.0	0.36	1.0081	1.0055	0.9985	0.73	0.69		0.03	0.927	0.72	8.28	1.22
e140228a	6.30	14.5	0.26	1.0037	1.0012	0.9985	0.52	0.70		0.04	0.929	0.87	5.33	1.27
e140326b	6.63	14.5	0.26	1.0046	1.0028	0.9987	0.69	0.55		0.02	0.937	0.58	3.63	0.67
e140715b	6.72	16.4	0.29	1.0088	1.0056	0.9986	0.69	0.66		-0.04	0.942	0.69	6.12	0.80
e140207a	6.67	10.0	0.18	1.0138	1.0081	0.9988	0.62	0.46	82.6	-0.20	0.948	0.51	2.56	0.42
e140723a	6.63	13.8	0.25	1.0119	1.0056	0.9985	0.52	0.66		0.03	0.952	0.79	5.13	0.75
e140423a	6.67	12.0	0.21	1.0101	1.0058	0.9986	0.63	0.52		0.03	0.956	0.56	3.70	0.70
e140516a	6.69	11.8	0.21	1.0053	1.0023	0.9986	0.56	0.61		0.00	0.962	0.69	4.02	0.66
e140718a	6.67	15.8	0.28	1.0156	1.0089	0.9986	0.60	0.70		0.01	0.962	0.77	5.89	0.88
e140227b	6.30	12.0	0.21	1.0028	1.0016	0.9984	0.73	0.56		0.01	0.964	0.57	3.85	0.79
e140514b	6.68	12.5	0.22	1.0035	1.0016	0.9986	0.63	0.51	129.7	0.01	0.973	0.55	3.44	0.72
e140731a	6.73	10.2	0.18	1.0102	1.0054	0.9984	0.594	0.72		0.07	0.978	0.78	8.27	1.17
e140731b	6.67	10.4	0.18	1.0060	1.0023	0.9985	0.503	0.52	134.9	-0.01	0.979	0.62	3.07	0.47
e140224b	6.61	15.0	0.27	1.0023	1.0017	0.9982	0.85	0.49	84.4	-0.06	0.980	0.44	3.36	0.53
e140409a	6.50	18.0	0.32	1.0188	1.0105	0.9980	0.60	0.67		0.08	0.983	0.73	6.60	1.09
e140501a	6.98	12.0	0.21	1.0072	1.0027	0.9985	0.48	0.54		0.02	0.983	0.63	3.94	0.63
e140729d	6.63	12.1	0.21	1.0101	1.0043	0.9985	0.505	0.57		-0.05	0.992	0.66	4.49	0.63
e140212b	6.70	10.0	0.18	1.0097	1.0055	0.9980	0.64	0.56	130.9	-0.06	1.000	0.57	3.54	0.61
e140518a	6.73	12.1	0.21	1.0034	1.0005	0.9984	0.43	0.62		0.00	1.006	0.77	3.56	0.70
e140724b	6.58	16.2	0.29	1.0199	1.0058	0.9987	0.34	0.77		0.00	1.018	1.08	7.04	1.00
e140310b	6.67	10.0	0.18	1.0083	1.0017	0.9983	0.34	0.62		-0.00	1.018	0.86	4.18	0.63
e140730a	6.75	14.2	0.25	1.0099	1.0038	0.9985	0.468	0.71		-0.02	1.025	0.83	5.49	0.87
e140312b	6.67	12.2	0.22	1.0037	1.0018	0.9984	0.63	0.60		0.01	1.029	0.60	4.59	0.87
e140730b	6.62	10.3	0.18	1.0148	1.0047	0.9984	0.383	0.61		-0.01	1.031	0.79	4.33	0.66
e140729b	6.63	17.1	0.31	1.0108	1.0035	0.9986	0.404	0.66		0.00	1.033	0.83	7.42	1.15
e140307b	6.67	13.0	0.23	1.0057	1.0017	0.9983	0.46	0.70		0.00	1.034	0.82	4.99	0.92
e140724c	6.58	15.8	0.28	1.0114	1.0030	0.9986	0.35	0.74		0.00	1.034	0.99	6.51	0.98
e140516b	6.67	14.0	0.25	1.0056	1.0015	0.9986	0.42	0.68		0.00	1.041	0.82	4.74	0.79
e140307c	6.67	12.0	0.21	1.0059	1.0008	0.9991	0.24	0.61		-0.01	1.044	0.96	4.58	0.78
e140310a	6.49	14.0	0.25	1.0052	1.0010	0.9984	0.37	0.57		0.00	1.056	0.73	4.94	0.89
e140516c	6.74	14.0	0.25	1.0064	1.0014	0.9986	0.36	0.57		-0.00	1.057	0.73	4.03	0.74
e140227a	6.32	9.5	0.17	1.0030	1.0013	0.9984	0.63	0.46	106.2	-0.02	1.065	0.46	3.13	0.69
e140214b	6.61	10.0	0.18	1.0077	1.0034	0.9976	0.58	0.51		0.00	1.068	0.51	3.46	0.77
e140724a	6.70	12.2	0.22	1.0199	1.0056	0.9987	0.33	0.70		-0.05	1.068	0.94	5.82	0.81
e140213a	6.67	10.0	0.18	1.0080	1.0043	0.9985	0.61	0.57		-0.03	1.069	0.56	3.43	0.50
e140514a	6.56	10.1	0.18	1.0038	1.0019	0.9985	0.64	0.59	134.8	-0.02	1.076	0.56	2.29	0.64
e140310c	6.56	12.3	0.22	1.0086	1.0018	0.9985	0.33	0.68		-0.05	1.076	0.90	5.81	0.81
e140721a	6.68	9.9	0.17	1.0194	1.0056	0.9985	0.339	0.65		-0.06	1.078	0.85	1.11	0.62
e140715a	6.61	10.0	0.18	1.0104	1.0032	0.9984	0.40	0.72		-0.04	1.080	0.86	5.25	0.56
e140307a	6.30	9.5	0.17	1.0062	1.0012	0.9985	0.35	0.74		-0.07	1.128	0.93	4.61	0.67
e140214a	6.61	10.0	0.18	1.0109	1.0040	0.9985	0.44	0.51	132.6	-0.08	1.138	0.55	2.60	0.46

Table B.1: Two-layer stratified ambient data

Bibliography

ADDUCE, C., LOMBARDI, V., SCIORTINO, G. & ROCCA, M. L. 2014 An improved two-layer shallow water model for the simulation of gravity currents moving on both flat and up-sloping beds. *J. Fluid Mech.* In Press.

ADDUCE, C., SCIORTINO, G. & PROIETTI, S. 2012 Gravity currents produced by lock exchanges: Experiments and simulations with a two-layer shallow-water model with entrainment. *J. Hydraul. Eng.* **138**, 111–121.

BAINES, P. G. 1984 A unified description of two-layer flow over topography. *J. Fluid Mech.* **146**, 127–167.

BENJAMIN, T. B. 1968 Gravity currents and related phenomena. *J. Fluid Mech.* **31**, 209–248.

BORDEN, Z. & MEIBURG, E. 2013 Circulation based models for Boussinesq gravity currents. *Phys. Fluids* **25**, 101301.

BRITTER, R. E. & LINDEN, P. F. 1980 The motion of the front of a gravity current travelling down an incline. *J. Fluid Mech.* **99**, 531–543.

CENEDESE, C. & ADDUCE, C. 2008 Mixing in a density driven current flowing down a slope in a rotating fluid. *J. Fluid Mech.* **604**, 369–388.

DAI, A. 2013 Experiments on gravity currents propagating on different bottom slopes. *J. Fluid Mech.* **731**, 117–141.

DAI, A. 2014 Non-Boussinesq gravity currents propagating on different bottom slopes. *J. Fluid Mech.* **741**, 658–680.

FLYNN, M. R., UNGARISH, M. & TAN, A. W. 2012 Gravity currents in a two-layer stratified ambient: The theory for the steady-state (front condition) and lock-released flows, and experimental confirmations. *Phys. Fluids* **24**, 026601, doi: 10.1063/1.3680260.

Grue, J., Jensen, A., Rusås, P.-O. & Sveen, J. K. 1999 Properties of large-amplitude internal waves. *J. Fluid Mech.* **380**, 257–278.

Härtel, C., Meiburg, E. & Necker, F. 1999 Vorticity dynamics during the start-up phase of gravity currents. *Il Nuovo Cimento* **22**, 823–833.

Härtel, C., Meiburg, E. & Necker, F. 2000 Analysis and direct numerical simulation of the flow at a gravity-current head. Part 1. Flow topology and front speed for slip and no-slip boundaries. *J. Fluid Mech.* **418**, 189–212.

Holyer, J. Y. & Huppert, H. E. 1980 Gravity currents entering a two-layer fluid. *J. Fluid. Mech.* **100**, 739–767.

Huppert, H. E. 1982 The propagation of two-dimensional and axisymmetric viscous gravity currents over a rigid horizontal surface. *J. Fluid Mech.* **121**, 43–58.

Huppert, H. E. & Simpson, J. E. 1980 The slumping of gravity currents. *J. Fluid Mech.* **99**, 785–799.

Keulegan, G. H. 1957 An experimental study of the motion of saline water from locks into fresh water channels. *Tech. Rep.* 5168. Nat. Bur. Stand. Rept.

Keulegan, G. H. 1958 The motion of saline fronts in still water. *Tech. Rep.* 5831. Nat. Bur. Stand. Rept.

Lane-Serff, G. F., Beal, L. M. & Hadfield, T. D. 1995 Eddy formation by dense flows on slopes in a rotating fluid. *J. Fluid Mech.* **292**, 39–53.

Lowe, R. J., Linden, P. F. & Rottman, J. W. 2002 A laboratory study of the velocity structure in an intrusive gravity current. *J. Fluid Mech.* **456**, 33–48.

Marleau, L. J., Flynn, M. R. & Sutherland, B. R. 2014 Gravity currents propagating up a slope. *Phys. Fluids* **26**, eid 046605, doi:10.1063/1.4872222.

Maxworthy, T., Leilich, J., Simpson, J. & Meiburg, E. H. 2002 The propagation of a gravity current in a linearly stratified fluid. *J. Fluid Mech.* **453**, 371–394.

Mehta, A., Sutherland, B. R. & Kyba, P. J. 2002 Interfacial gravity currents: Part II - Wave excitation. *Phys. Fluids* **14**, 3558–3569.

Meiburg, E. & Kneller, B. 2010 Turbidity currents and their deposits. *Annu. Rev. Fluid Mech.* **42**, 135–156.

Munroe, J. R., Voegeli, C., Sutherland, B. R., Birman, V. & Meiburg, E. H. 2009 Intrusive gravity currents from finite-length locks in a uniformly stratified fluid. *J. Fluid Mech.* **635**, 245–273.

Rottman, J. W. & Simpson, J. E. 1983 Gravity currents produced by instantaneous releases of a heavy fluid in a rectangular channel. *J. Fluid Mech.* **135**, 95–110.

Rottman, J. W. & Simpson, J. E. 1989 The formation of internal bores in the atmosphere: A laboratory model. *Q. J. R. Meteorol. Soc.* **115**, 941–963.

Shin, J. O., Dalziel, S. B. & Linden, P. F. 2004 Gravity currents produced by lock exchange. *J. Fluid Mech.* **521**, 1–34.

Simpson, J. E. 1972 Effects of the lower boundary on the head of a gravity current. *J. Fluid Mech.* **53**, 759–768.

Simpson, J. E. 1982 Gravity currents in the laboratory, atmosphere, and ocean. *Ann. Rev. Fluid Mech.* **14**, 213–234.

Simpson, J. E. 1997 *Gravity Currents*, 2nd edn. Cambridge, England: Cambridge University Press.

Sutherland, B. R., Barret, K. J. & Ivey, G. N. 2013*a* Shoaling internal solitary waves. *J. Geophys. Res. Oceans* **118**, 4111–4124, doi:10.1002/jgrc.20291.

Sutherland, B. R., Kyba, P. J. & Flynn, M. R. 2004 Interfacial gravity currents in two-layer fluids. *J. Fluid Mech.* **514**, 327–353.

Sutherland, B. R., Polet, D. & Campbell, M. 2013*b* Gravity currents shoaling on a slope. *Phys. Fluids* **25**, 086604.

Tan, A. W., Nobes, D. S., Fleck, B. A. & Flynn, M. R. 2010 Partial depth gravity currents in two-layer stratified media. Part 1: A study of the wave amplitude. In *International Conference on Environmental Science and Engineering*, p. SG69000. WASET.

Ungarish, M. 2009 *An Introduction to Gravity Currents and Intrusions*. New York: Chapman and Hall/CRC press.